Final Technical Report

Award: G14AP00100
Title: Development of 3-D Q Model for Regional Attenuation in Northern California

Donna Eberhart-Phillips
Earth and Planetary Sciences Department
University of California Davis
1 Shields Ave.
Davis, CA 95616

530-771-7241 (tel), 530-752-0951 (fax), eberhartphillips@ucdavis.edu (email)

Start: Aug. 1, 2014
End: Nov. 30, 2016

The results of this project are in press in BSSA:
Eberhart-Philips, D. (2016). "Northern California seismic attenuation: 3-D Qp and Qs models." Bull. Seimol. Soc. Am. *in press*.
This includes an electronic supplement of the 3D model that can be used in other applications.

ABSTRACT

The geological complexity of Northern California, and its accreted terranes, produces pronounced regional variations in the attenuation (1/Q) of earthquake waves. Using local earthquakes, 3-D Qp and Qs models have been obtained for this region which includes the San Andreas fault system, the Great Valley, the Sierra Nevada batholith, and the Gorda subduction volcanic system. Path attenuation t* values were determined from P and S spectra of 959 spatially distributed earthquakes, magnitude 2.5-6.0, using 1254 stations from NCEDC networks and Mendocino and Sierra Nevada temporary arrays. The t* data were used in Q inversions, using existing 3-D velocity models and basic 10-km node spacing. Uneven data coverage was accommodated with linking nodes into larger areas for useful Q images across the 3-D volume. Results at shallow depth show very low Q in the Sacramento Delta, the Eureka area, and parts of the San Francisco Bay Area. In the brittle crust, low Q tends to be associated with regions of fault zones and microearthquakes. In the ductile lower crust, low Q is observed below fault zones with large cumulative displacement and inferred grain size reduction, with apparent broad ductile shear zones across the fault system in the Coast Ranges. Underlying active arc volcanoes, low Q features are apparent below 20-km depth. Under Long Valley caldera, two distinct partial melt features at ~3 km and ~15 km depth are inferred. Moderately high Q is associated with Sierra Nevada and Salinian igneous rocks, while the Franciscan subduction complex shows moderately low Q. Prominent high Q relates to the Great Valley Ophiolite. The pattern of path specific attenuation rate, from 3-D Q, is generally similar to the pattern of psuedospectral acceleration residuals for the South Napa earthquake, indicating that it may be beneficial to incorporate 3-D Q models into future GMPEs for northern California.

INTRODUCTION

This study aims to obtain useful 3-D Qp and Qs models throughout northern California. Q describes attenuation where 1/Q is the fractional loss of energy per cycle. Attenuation may be related to lithology, deformation, fluid and thermal effects. Considering these factors, Q patterns may differ from patterns in seismic velocity, and provide new insights. This region has diverse geologic terranes and complex deformation processes that will result in pronounced heterogeneity in Q, such that attenuation will vary greatly for different paths from a source. Thus obtained 3-D Q models will be useful for incorporation into a regionally adjustable ground-motion prediction equation (GMPE) such as Yenier and Atkinson (2015). GMPEs are a key tool for ensuring safe structures in seismically active regions such as northern California.

In the brittle crust attenuation results from viscous damping of local pore fluid motion and grain boundary frictional sliding (Winkler and Murphy, 1995). Negligible attenuation occurs in impermeable rock, while attenuation increases for increased porosity as found in sedimentary rock, and increased temperature as found in volcanic areas. Zones of distributed fractures are effective in decreasing Q with a linear relationship between 1/Q and crack density (Peacock et al., 1994), and increased fluid pressure may further reduce Q. Scattering attenuation also occurs in heterogeneous rock and may contribute roughly equally to intrinsic attenuation (Frankel, 1991). The broad regions of microcracks around active fault zones and areas of microearthquakes may exhibit low Q, resulting from both fractures and fluids. The fractures will produce scattering as well as increased porosity and permeability. Low Q and scattering have been observed in fault and fracture regions in other areas. In the region of the Mw 7.3 western Tottori earthquake, Asano and Hasegawa (2004) found a prominent S scattering zone along and around the fault zone down to 20 km depth. In this region there are zones of lineaments but no major mapped fault and the scattering was attributed to fluid-filled cracks and heterogeneous structure. In the region of the North Anatolian fault zone (NAFZ), Koulakov et al. (2010) found the lowest Q at 5 km depth in sedimentary basins, and low Q at 10-20 km depth correlated with fracturing zones of the NAFZ which had large earthquakes in the 20th century, although the central section had moderately-high Q. Ma (2008) numerically models the material response to fault rupture and finds that most damage occurs from seismic energy radiated from the fault ahead of the rupture front, with the damage zone becoming very broad within 2 km of the surface. Mitchell and Faulkner (2008), in experimental studies, found that the permeability of the fault tip process zone increases by 2 orders of magnitude, and that new microcracks and permanent strain occur during cyclic loading. These studies are consistent with a relationship between high attenuation and high fracture connectivity in areas of recent seismicity, and the lack of such attenuation associated with locked fault zones that have little seismicity.

In the ductile crust, Q is influenced by temperature, grain-size, water, and mineral content. The attenuation results from recoverable grain-boundary sliding which is affected by grain size, and hence grain-size reduction from long-term high strain rate will greatly reduce Q (Jackson et al., 2002). In high stress and low temperature regions, increased strain rates produce grain-size reduction (e.g., White et al., 1980; Platt and Behr, 2011), and thus high strain zones in the ductile crust should exhibit low Q. Ductile high-strain zones of shear localization may be <1 km-100 km wide, typically widening with depth (e. g., Norris and Cooper, 2003). Grain-boundary sliding is also enhanced by the presence of water reducing grain-boundary viscosity, and hence the presence of water can also reduce Q (Aizawa et al., 2008; Karato, 2012).

The geology of northern California is summarized below and in Figure 1, following Irwin (1990). The Sierra Nevada is a Late Triassic to Late Cretaceous large granitic batholith with a metamorphic belt of island arc rocks and plutons (Schweickert, 1981). In northernmost California, the Klamath mountains consist of Paleozoic and Triassic metasedimentary and

metavolcanic rocks (Scherer and Ernst, 2008), and the Modoc plateau includes Cenozoic flood basalts (McKee et al., 1983). On the southwest side of the San Andreas fault (SAF), the Cretaceous Salinian terrane contains granitic and metamorphic rocks (Page, 1981). The Franciscan is an uplifted Late Jurassic to Miocene accretionary wedge terrane composed of greywacke mélange with some volcanics and chert (Blake et al., 1988). The Cenozoic and Mesozoic Great Valley sequence (GVS) formed as an over 12-km thick sedimentary forearc basin (Ingersoll, 1982; Wentworth et al., 1995).

The underlying oceanic crust remains as the ultra-mafic Great Valley ophiolite (GVO) which has been obducted onto Sierra Nevada batholith on the eastern side of the Great Valley, and the fragmented Coast Range ophiolite (CRO) which separates the GVS and the underthrust Franciscan terrane on the western side of the Great Valley (Godfrey et al., 1997; Moores et al., 2002). Godfrey and Klemperer (1998) have analyzed seismic and potential field data for 18 profiles across the GVO, and their generalized sections for the Sacramento and northern San Joaquin basins are shown in Figure 1b-c. Their interpreted GVO has 10-20 km thickness, including mantle rock on some sections.

Deformation in northern California is dominated by transform motion along a broad SAF system approximately ~100-km wide. This incorporates secondary subparallel faults located northeast of the SAF in northern California and southwest of the SAF in central California. The measured deformation field across the region has roughly 60% of the strike-slip on the SAF, and may be fit by various models ranging from discrete faults to distributed deformation (Kenner and Segall, 2003; Yikilmaz et al., 2015). The margin of the Great Valley limits the broad shear zone, and the Great Valley-Sierra Nevada behaves as a strong coherent block, which has been described as a microplate (Argus and Gordon, 2001). The SAF ends at the Mendocino triple junction (MTJ), with the northern region dominated by the eastward subduction of the Gorda plate, which drives volcanism along the southern Cascade arc volcanoes (Mt Shasta, Mt Lassen). The subducted edge of the Gorda plate has been inferred by Liu et al. (2012) to extend under California to Lake Tahoe (dashed line, Figure 1). The region north of San Francisco has been influenced by the northward movement of the MTJ over the last ~5 My, leaving thinner lithosphere and periodic magmatism (Furlong and Schwartz, 2004).

To date, existing studies of Q in northern California highlight the region's geological complexity. In the Loma Prieta region, Lees and Lindley (1994) showed low Q in a marine sedimentary basin southwest of the SAF and high Qp and low Qs in the deep aftershock zone. In the Parkfield region, Bennington et al. (2008) found low Q in sedimentary rock and high Q in Salinian basement. Phillips and Stead (2008) determined Q throughout the western US from Lg data and showed very high Q in the Sierra Nevada batholith and relatively low Q throughout the SAF transform region. Lin (2014) determined 3-D Qp for northern California using permanent network data, and found low Qp along fault zones and near Mendocino, and imaged the SAF as a

Q boundary in central California. Regional 3-D seismic velocity models are available from Thurber et al. (2009) for northern California and Lin et al. (2010) for all of California. Both show patterns related to geology and fault zones. We utilize the larger velocity model (Lin et al., 2010) in our computations.

DATA

For analysis of t*, desirable data has sufficient signal-to-noise ratio over the 1-25 Hz frequency range for numerous stations, and events with magnitude greater than 2.5 are usually adequate. Smaller magnitude events may have a limited number of adequate waveforsm, but those might be biased toward high Q. To obtain a useful 3-D image, relatively even spatial distribution is desirable, which may be achieved by incorporating temporary stations and selecting distributed events rather than including numerous redundant events. Considering magnitude and periods of network coverage, 959 spatially distributed earthquakes, with magnitude 2.5-6.0, were selected for the period January 2005 – September 2014. The majority of waveform data were obtained from the Northern California Earthquake Data Center (NCEDC), which includes broadband and short-period data from the U. S. Geological Survey (USGS), University of California Berkeley (UCB), and EarthScope. The EarthScope transportable array ran from 2005-2007. Data were also obtained from the USGS Delta seismic array (UDSAR) which operated from 2006 to 2014 (Fletcher and Boatwright, 2013). Additional temporary network data were obtained from IRIS from two experiments. The large Sierra Nevada EarthScope Project (SNEP) broadband array operated May 2005-October 2007 and has been used to determine variations in lithosphere properties from surface wave data (Gilbert et al., 2012). The Flexible Array Mendocino Experiment (FAME) operated July 2007 – December 2012 and has been used to image heterogeneity of the lithosphere and asthenosphere related to the Mendocino triple junction from ambient noise and receiver functions (Liu et al., 2012). Figure 2 shows the stations and earthquakes included in this study, which uses both vertical and horizontal components. Hypocentral locations were extracted from the double-difference catalog (Waldhauser, 2009). Arrival times are required for selecting the time windows for spectral analysis. Catalog arrival times for the NCEDC data were used and most Delta array arrival times were hand-timed (Teel, 2012). Most arrivals from the SNEP and FAME records were hand-timed, and an autopicker was applied for any records that did not have associated arrival times.

METHOD

Fitting spectra for t*

Q describes attenuation where 1/Q is the fractional loss of energy per cycle. As such, high Q indicates low attenuation and low Q indicates high attenuation. Q may exhibit frequency (*f*) dependence with an exponent α,

$$Q(f) = Q_{f0}(f / f_0)^{\alpha} \quad (1)$$

where f_0 is a reference frequency, taken as 10 Hz in this study. A frequency dependence (α) of 0.5 is used here, following a previous evaluation of northern California attenuation (Eberhart-Phillips et al., 2014b), and the 1-25 Hz frequency band is examined in this study.

The parameter t* describes the whole path attenuation, and when Q and V vary spatially, t* is related to Q by

$$t^* = (f/ f_0)^{-\alpha} [\int_{ray} ds /[Q_{f0}(s)*V(s)] + t^*_{station}] \quad (2)$$

Hence t* data from local earthquakes are amenable to inversion for 3-D Q (Rietbrock, 2001), where $t^*_{station}$ are station terms that can be included in the inversion. Assuming the frequency-dependence does not vary spatially, we include a frequency-dependent term when fitting the spectra and so determine frequency-dependent t* data, $t^*_{\alpha f0}$.

$$t^*_{\alpha f0} = (f/ f_0)^{\alpha} [t^*_f] \quad (3)$$

The $t^*_{\alpha f0}$ data can then be used in inversion for Q_{f0}, and we will refer to that data as our t* data. In this study, frequency dependence is applied using α =0.5 and f_0= 10 Hz. Comparing t* data for α=0 to those for α=5 for northern California, Eberhart-Phillips et al. (2014b) showed a strong linear relation with $t^*_{\alpha 5} \sim 1.8\ t^*_{\alpha 0}$, such that for the frequency dependent 3-D models computed in this study, frequency independent $Q_{\alpha 0}$ would be ~1.8 $Q_{f10\alpha 5}$ with similar patterns of Q heterogeneity.

The velocity amplitude spectra are used to obtain the t* data.

$$A_{ij}(f) = 2\pi f \Omega_0 * \frac{f_c^{\,2}}{\left(f_c^{\,2} + f^2\right)} * \exp[-\pi f (t^*_{ij})] T_j(f) \quad (4)$$

The observed spectra $A_{ij}(f)$, for the event *i* at the station *j*, is fit with three parameters (Ω_0, f_c, and t*). The low-frequency spectral level, Ω_0 is proportional to seismic moment and here incorporates the frequency independent geometrical spreading. The corner frequency, f_c, and t* are determined assuming an ω^2 source model (Brune, 1970).

For a given f_c, each velocity spectrum is fit by nonlinear least-squares for Ω_0 and t* (Wang et al., 2009), using the portion of the 1-25 Hz frequency band that has signal-to-noise ratio (S/N) over 1.25. An example is shown in Figure S1 (available in the electronic supplement to this article). The best-fitting corner frequency, f_c, of the event is estimated by a grid search over an f_c range based on values approximated for 1-25 MPa stress drop across a circular fault (Abercrombie, 1995). In order to weight each t* residual in the Q inversion, a quality is

estimated for the t* observation based on how well the spectrum is modeled, the range of frequency that is modeled, and the proportion of the range that has S/N >2.3.

The site response, $T_j(f)$, incorporates local effects that are common to all earthquakes at a specific station. First, t* for all events are obtained without site response. Then station site response values are determined by averaging together all the residuals for each station, using a 5-point moving average and limiting the effect of high residuals and cases where there are few adequate signal-to-noise ratio (S/N) observations. The site response correction has no systematic effect on the t* values, since it is calculated from the residuals and can be negative as well as positive. Final t* values after removal of site response have improved misfit and better quality for the Q inversion.

For P-data, t* estimates are obtained from a 2.5 s window starting at the P-arrival. An alternate method is used for S wave data, since there are fewer clear S-arrivals and they are biased to representing higher Q paths. Useful S t* estimates have been selected within a -2 to 16 s window around a predicted S arrival, using the 5-95% energy integral, and using a noise window 3-0.5 s prior to the P-arrival to compute S/N (Suppl. Fig. 1; Eberhart-Phillips et al., 2014b). Spectra are fit over the frequency range that has S/N over 1.25, with clipped data removed. In total, this study uses 85,548 P t* data and 201,181 S t* data. The S t* include both horizontal and vertical components.

<u>3-D Q inversion</u>

The t* data were used in inversions for 3-D Qp and Qs (Rietbrock, 2001; Eberhart-Phillips and Chadwick, 2002) with raypaths determined from the pre-existing 3-D velocity model. The solution is obtained by iterative damped least squares, with the damping parameter for each inversion chosen empirically by evaluating a trade-off curve of data variance and solution variance. We excluded physically unrealistic negative t* data. The inversion algorithm (Eberhart-Phillips and Reyners, 2012) used here incorporates receiver-differential t* values (rdt) between two stations for the same earthquake, along portions of raypaths near stations which provide more detailed resolution on the receiver side; and similarly earthquake-differential t* values between two earthquakes for the same station, along portions of raypaths near groups of earthquakes. The 3-D velocity is taken from a well-constrained regional study (Lin et al., 2010). We utilized an appropriate 3-D initial Q model for northern California that was previously obtained with Q as a function of V (Eberhart-Phillips et al., 2014b).

The distribution of the S t* data is shown in Figure 3a-c with plots of the derivative weight sum (DWS, Thurber and Eberhart-Phillips, 1999) accumulated along raypaths at nodes of a 10-km grid. With local earthquake data, the data coverage is uneven although all areas have some raypaths except a shallow swath along the San Joaquin valley where there are no stations

(Figure 2a). At 1-km depth, the near-surface DWS is low and patchy where there few hypocenters and regions between stations are not sampled. The DWS is largest at hypocentral depths in areas with the most seismicity, such as at 8-km depth in the Bay Area. The lower crust, at 20-km depth, is widely sampled by downgoing raypaths toward distributed stations. To improve shallow resolution, receiver-differential times are included which increase DWS in most locations (Figure 3d). Earthquake-differential times (*edt*) are also included to improve sampling of the lower crust and to help reduce smearing of velocity perturbations along raypaths through assigning some common event differential residuals to the portions of the raypaths closer to the hypocenters. For *edt* observations, a minimum path length of 75-km is used to improve DWS along longer downgoing raypaths, which gave 5358 S and 7688 P t* *edt* observations. The improvement in DWS at 20-km depth is shown in Figure 3f where a much larger region has DWS greater than 1000.

With the goal of obtaining a reasonable Q model everywhere despite the varied data distribution, a series of inversions was performed with increasing complexity. Station t* terms were included. Autolinking was employed to effectively have varied size areas related to inversion nodes and thus provide relatively even resolution (Eberhart-Phillips and Reyners, 2012). For given *dx* and *dy* parameters, the area was split into boxes sized 3-*dx* by 3-*dy* and the associated nodes were evaluated for linking such that low DWS nodes (<*dwslo*) were linked together if the combined DWS is less than a cutoff value. To avoid arbitrary patterns related to linking, nine autolinking runs were performed for the nine possible autolinking patterns. Next, the nine varied 3D Q results were averaged together. Considering that tectonic features generally align in the y direction (Figure 1), the first inversions developed a moderately coarse model, using autolinking with *dx*= 20 km, *dy* =30 km and *dwslo*= 800, such that the maximum linked areas were 60-km *x* by 90-km *y*. More detail could be obtained in many areas that had abundant data, so finer-scale inversions were done using the coarse model as their starting model. The fine autolinking used *dx*= 10 km, *dy* =10 km and *dwslo*= 100, such that the maximum linked area was 30-km *x* by 30-km *y*. Lastly, using the fine-scale averaged model, a final inversion was done for the shallowest material and station t* terms.

The coarse 3-D Qp inversion model achieved a 45 % reduction in data variance from the initial 3-D model, and the fine 3-D inversion Qp model achieved a further 6% reduction, giving a total 51% reduction in data variance. For Qs, the coarse 3-D inversion achieved 48 % and the fine 3-D achieved 8 %, for a total 56 % reduction in data variance from the initial 3-D Qs model. As the initial 3-D Q models used Q as a function of velocity, the large improvements in data variance confirm that many factors have significantly greater or different influence on Q than velocity, and thus there is not a reliable systematic relation between the parameters.

RESULTS

The final 3-D models for Qs and Qp are shown in mapview from 1 to 27 km depth in Figures 4 and 5. Broad trends reveal higher Q in the Sierra Nevada than along the SAF system, lower Q along the northern region and above the subducted slab, and high Q related to some tectonic blocks and terranes.

The sharpness and detail of the 3-D image spatially correlates with the data distribution. Hence where there is high DWS (Figure 3), 10-km wide zones (i.e. node spacing) are imaged. Where there is moderately low DWS, broader Q features could possibly represent narrower zones. The resolution is illustrated by the spread function (SF) (Michelini and McEvilly, 1991) for a non-linked 30-km grid inversion (Figures S1, S2, available in the electronic supplement to this article). Based on the resolution matrix, the SF describes how strong and peaked the resolution is at each location. The resolution is good, with little smearing of features, where SF is low. In areas with moderately high SF (>3), the Q pattern is reasonable, but the shape of features and specific Q values are weakly constrained, and there may be additional detail that has not been imaged. For SF > 3.5, there is little resolution and only coarse broad features may be imaged with poor definition of their shape or extent. The images in the Q plots (Figures 4-8) have pale lines for the SF=3.5 contours. The resolution is best where there are numerous earthquakes and stations, and the northern SAF image is thus not as detailed as the central SAF image. Most of the area has adequate resolution at 20-km depth. At 1-km depth the resolution is patchy and there is little resolution of the shallow southern San Joaquin valley since it lacks stations.

The 3-D Q models and SF values are listed in Table S1 (available in the electronic supplement to this article). Station t* terms were included in the inversions and are shown in Figure S4 (available in the electronic supplement to this article). As the structure is included in the 3-D Q models, the station terms are near zero, do not show spatial patterns, and may be positive or negative as needed to fit some stations. Note that this approach is different from the GMPE κ_0 site terms which are defined to be all positive and to relate to uniform Q models.

DISCUSSION

Terranes and geology

Some features of the 3-D Q models may be related to the varied terranes and geologic provinces that make up California (Figure 1). The Sierra Nevada has moderately high Q from 1-27 km depth, with Qp and Qs ~300-600 (Figures 4-5). This is consistent with the large coherent structure of relatively unfractured metamorphic and igneous rock with low porosity, which hence has little attenuation. The Salinian terrane, located west of the SAF, is a batholithic terrane that similarly has high Qs from 1-14 km depth. This has a section of lower Q that spatially correlates

with seismicity, and thus may be associated with micro-fractures and fault networks. The Modoc Plateau in northeastern California has intermediate Q (~300) in the upper crust, 4-8 km depth.

The Franciscan terrane subduction complex, which lies in regions northeast of the SAF and south of the Salinian block, has moderately low Q, ~200 at 8-km depth (compare Figure 4c to Figure 1a). The moderately low Q region also characterizes the adjacent Great Valley sequence (GVS) forearc sedimentary rock located east of the Coast Ranges. These sedimentary rocks have relatively higher porosity, fluid content and fracturing that produce greater attenuation. The Franciscan in the San Francisco Bay area is disrupted by the strike-slip fault system, with a relatively narrow block of coastal Franciscan east of the San Andreas fault. In this region, Holbrook et al. (1996) find a mafic lower crust from ~15-25 km depth that may be underplated basalt or stalled subducted oceanic crust (Godfrey et al., 1997). Its reflectivity led them to infer that it has undergone extensive shear deformation. The 3-D Q results find moderately high Q (300-600) for the Bay Area block in the 4-14 km depth range (Figure 6b-c). This block between the San Andreas and Hayward faults lacks seismicity and the moderately high Q is consistent with a strong unit having relatively low fracture density.

Great Valley Ophiolite

The Great Valley ophiolite (GVO) is a block of oceanic plate that collided with the continent and was obducted up on the continent (Moores et al., 2002). Its lateral and depth extent have been studied by Godfrey and Klemperer (1998). They find it thickens to the north under the Sacramento basin and includes both oceanic crust and mantle (Figure 1b). In the Sacramento basin, they interpret ~70-km wide GVO underlying much of the GVS. Under the eastern Great Valley, the GVO is a 10-km thick layer above thick Sierran crust. Under the central and western Great Valley, the GVO is inferred to thicken to 25-km by incorporating GVO mantle. We image this with high Q from 14-27 km depth (Figure 4d-f; Figure 7a-c). It is a narrow feature at 27-km depth that seems to end in the southern Sacramento valley. In the northern San Joaquin valley, Godfrey and Klemperer (1998) show slightly shallower 10-km thick GVO, without ophiolite mantle and thus Sierran basement extends across under the western Great Valley in that area (Figure 1c). This is consistent with our results, where very high Q is not imaged from y=200 to 100 for 20-27-km depth (Figure 4e-f). In the southern San Joaquin valley (y=75 to -75), some high Q is imaged below the western margin at 14-27-km depth (Figure 7g-h), where Godfrey and Klemperer (1998) also infer thicker mafic material.

Shallow Crust

The results at shallow depth (< 2 km) show very low Q (<50) in the Eureka forearc area (Figures 4a, 5a), the Sacramento-San Joaquin Delta, and parts of the Bay Area (Figure 6). The low Q is consistent with thicker alluvium and permeable, relatively high-porosity sedimentary

rock. The Delta is a broad low-lying area across which the Sacramento and San Joaquin rivers merge and empty into San Pablo Bay, and contains thick sediments with peat soils. Fletcher and Boatwright (2013) studied the Delta array and observed basin waves generated at the edge of the basin, and determined that the upper 2 km has Vs of 0.3-1.1 km/s, due to weak peat, eolian, and fluvial sediments. The lowest Q areas are in the central Delta and northeast of Mt. Diablo. Fault structures and sub-basins have been inferred in the Delta (Beyer, 1988), and the discrete areas of extremely low Q (<25) may be related to such features where we have adequate station density. There appears to be an arch-like feature of slightly higher Q along the Greenville fault and extending to Mt. Diablo. This feature is similar to higher velocity features within the Delta ambient noise study of Fletcher et al. (2016).

In the Eureka area, there is a large region of shallow low Q, consistent with weak sedimentary material in the forearc (EB, Figures 4a, 5a, 8b). Here the large Eel River forearc basin extends 50 km onshore, and 150 km offshore of northern California and southern Oregon, and also exhibits very low velocity, with Vp < 4 km/s to ~5km depth (Beaudoin et al., 1994; Thurber et al., 2009). The Eel River basin developed in the Neogene, and incorporates marine sedimentary rocks ~4 km thick, with folding and imbricate thrust faults that may sole into the plate interface (Clarke, 1992; Hopps and Horan, 1983).

Along the SAF system, there is a region of shallow low Q northeast of the Rodgers Creek fault and southwest of the Green Valley fault (Figure 6a-b). This may be related to weak sedimentary rocks in some basins along faults (McPhee et al., 2007; Brocher et al., 2015), as well as abundant micro-cracks in geometrically complex fault regions. The low Q zone extends to the fault junction region of the Hayward and Calaveras faults, where Thurber et al. (2009) show low Vp. Particularly low Q occurs at the northern end of the Calaveras fault, west of the uplifting Mt. Diablo. There may be some subsidence and weak sedimentary rocks in this step-over region, with fracturing across the distributed structures.

Fault Zones

In the brittle crust regions with active faults tend to have low Q, particularly where there is high seismicity (Figures 4b-d, 5b-d). With the 10-km grid, the 3-D Q model is not examining the narrow fault surface, and the gridpoints are not directly centered at mapped fault segments. This low Q may relate to microcracks in a broad zone around the fault in contrast to locked sections where fractures are healed. For example, near the SAF in Parkfield, Audet (2015) finds that upper crustal fracture-induced anisotropy extends > 3 km away from the fault zone seismicity, and to ~8 km depth. This Q pattern is similar to the South Island, New Zealand, where upper crustal low Q is located in regions that have a high level of background seismicity, while the locked Alpine fault is apparent as a crustal boundary but lacks distinctive low Q in the brittle crust (Eberhart-Phillips et al., 2008a, 2014a). Small magnitude earthquakes may produce

broad microfracture areas of high crack density and permeability even though they do not have large slip. If fluid is present, it can enhance attenuation across areas of high crack density.

The crustal thickness under the SAF is approximately 25-km, deepening toward the northeast (Tape et al., 2012), and seismicity tends to occur above 15-km depth. Hence the ductile lower crust is imaged in the 20-27 km depth grids (Figures 4e-f, 5e-f). This shows lower Q under the major faults which have large cumulative displacement, as expected for long-term shear zones with grain-size reduction. Q is greatly influenced by grain size, such that Q is roughly proportional to $d^{1/n}$, where d is grain size and n is a power exponent that depends on temperature and mineralogy (Jackson et al., 2002). In high stress and low temperature regions, increased strain rates produce grain-size reduction through strain energy driven grain-boundary migration (e.g., Platt and Behr, 2011), and thus high strain zones in the ductile crust should exhibit low Q. Shear zones typically widen with depth, and numerical modeling shows localized strain zones extending to and linking within the base of the crust above a strong mantle (Ellis et al., 2006; Eberhart-Phillips et al., 2014a).

Cross-sections are shown in Figure 7. In the north, y= 400 to 310 (Figure 7a-c), the Maacama, Bartlett Springs, Rodgers Creek and Green Valley fault zones are apparent, while there is less resolution of the SAF. These fault zones tend to have distinct low Q in the upper crust, while at 14-20 km depth, the low Q extends across the region between the faults. Northeast of the fault system, there is deep seismicity (20-30 km depth) that appears associated with the high Q GVO.

In the Bay Area (Figure 7d-e, y=250, 190; Figure 6), the SAF, Hayward and CGVF are distinct features with the SAF and Hayward faults separated by the moderately high Q Bay Area block from 4-14 km depth. At 20-km depth, moderately low Q extends across the faults and suggests the entire lower crust serves as a distributed shear zone, consistent with Holbrook et al. (1996) reflectivity results.

At the junction of the SAF and Calaveras fault (Figure 7f, y=100), there is a pronounced low Q zone in the brittle crust and broad moderate low Q in the ductile crust on both sides of the SAF region. Along the central SAF (Figure 7g-h, y=10, -50), the SAF has a shallow low Q region and a sharp Q boundary in the brittle crust with the high Q Salinian igneous rock on the southwest. The Rinconada and San Gregorio-Hosgri faults also have some expression of low Q where there is seismicity. In the lower crust, the low Q zone extends southwest of the SAF under these faults, in opposite sense to the Bay Area. The lateral extent of moderately low Q ductile lower crust thus appears related to the location of the northern and southern Coast Ranges (Figure 1), which may have crustal rheology favorable to development of secondary faults. Fluid-saturated metasedimentary crust deforming through grain-size sensitive creep may produce a broad shear zone that widens from 10 to 100 km at the base of the crust (Platt and Behr, 2011).

The adjacent margin of tectonic wedging and GVO basement may provide a different rheology less favorable to such strain localization. Near Parkfield, Audet (2015) finds a mid-crustal (~8-20 km depth) anisotropic layer consistent with pervasive highly foliated mica schists and fluid-rich shear zones, and notes that differing patterns of anisotropy on the northeast may indicate contrasts in strength across the fault. Underlying the anisotropic mid-crust, Audet (2015) determines an ~15 km thick lower crust that lacks anisotropy.

In the Parkfield section (y=10 to -60), there is a large area of low Q southeast of the SAF, with lowest Q within 10-km of the fault from 4-8 km depth (Figure 7g-i). This is consistent with seismic velocity and resistivity models which suggested a large volume of saline overpressured GVS material (Eberhart-Phillips and Michael, 1993). At 8-14 km depth, low Q extends southeastward across the Coalinga-Kettleman Hills region of active seismicity. In this area northeast of the SAF, there is low Q and seismicity related to the Coalinga-Kettleman Hills thrusts, and the seismicity continues into high Q mafic lower crust (y= -50, Figure 7h). This deep seismicity is similar to that seen near the GVO in the northern Sacramento valley (y=400, Figure 7a), and conveys a large change in rheology across the SAF with the brittle-ductile transition deepening on the northeast to ~30 km with a relative lack of ductile lower crust.

In the upper mantle, the SAF low Q zone extends to 45-km depth, is centered under the SAF, and is narrower than in the overlying lower crust. The deep low Q fault zone is apparent from y= 190 to -100 (Figure 7e-g). There is less uniform resolution at 35-45 km depth (Figure S2, available in the electronic supplement to this article), and hence the spotty image of SAF upper mantle low Q could represent a more continuous feature along the fault. This deep zone is consistent with the San Andreas fault zone being a lithospheric plate boundary, and the secondary faults may not be lithospheric faults. Waveform modeling along California shows a sharp change in lithospheric structure across the SAF with a fast thick seismic lid in the Pacific plate upper mantle providing strength to the Pacific lithosphere relative to the North American plate (Lai et al., 2015). The North American plate will be particularly weak in the northern section near the Maacaama fault and Clear Lake, where the slab gap has thinned the lithosphere.

Subduction System

The eastward subduction of the Gorda plate and northward migration of the MTJ exert primary influence in the northern part of California, including the Lassen and Shasta volcanoes. The lithosphere and asthenosphere structure has been studied by Liu et al. (2012) using surface waves and receiver functions. They image the slab to 100-km depth and determine that the southern slab edge extends from the MTJ to south of Lake Tahoe (Figure 1). They determine low Vs partial melt at 60-80 km depth beneath the arc volcanoes, and shallow lithosphere (30-40 km depth) in the region south of the slab edge.

Q cross-sections of this region are shown in Figure 8. The slab is a very high Q feature (Qs>1200), with a broad low Q region in the overlying forearc crust. Subducted slabs are strong relatively homogeneous elastic features that effectively transmit seismic energy, and are typically imaged with similarly high Q (Stachnik et al., 2004; Eberhart-Phillips et al., 2008b).

The shallow crust under the volcanoes has low Q and there is moderately low Q throughout the arc crust and upper plate from 20-45 km depth, with lowest values (<200) at 20-km depth. This low Q extends to the southern slab edge, similarly to the low Vs mantle wedge shown by Liu et al. (2012), and the decreased Q may be attributed to fluids associated with slab dehydration.

The northwestward migration of the MTJ includes the subducted Gorda slab and hence leaves a gap in its wake described as a slab window (Furlong and Schwartz, 2004) into which flow sub-Gorda asthenosphere and abandoned mantle wedge asthenosphere (Liu et al., 2012). This has resulted in volcanism and intrusion in the northern Coast Ranges, with the most recent in Lake Pillsbury north of Clear Lake (Levander et al., 1998) which is located adjacent to the current slab edge. This location has distinct low Q at 20-km depth (Figure 4e) that continues to 35-km depth, the extent of resolution. In cross-section (Figure 7a) this ~70-km wide low Q upper mantle is centered under Lake Pillsbury and seismicity along the Bartlett Springs fault zone.

Long Valley Caldera

Long Valley Caldera is a volcanic center in the southern Sierra Nevada (Figure 1) which is characterized by earthquake swarms and episodes of Caldera uplift (Hill, 2006). Lin (2015) has determined an aseismic low Vp high Vp/Vs body 1-4 km depth which represents partial melt consistent with inflation models. In the underlying mid-to-lower crust, a magma chamber has been imaged as a broad low Vp feature centered at 15-km depth (Thurber et al., 2009). Partial melt causes large attenuation, and the 3-D Qs model shows discrete low Qs related to these magmatic features (Figures 8d). The shallow low Qs feature occurs 1-4 km depth under the caldera, with Qs <100 at 1-km depth. At 8-km depth there is moderately high Qs similar to the surrounding Sierra batholith, and then at 14-km depth, there is a small low Qs region with Qs <200. This feature is under the caldera and does not extend southeast across the band of seismicity, and it does not extend to 20-km depth.

Path-averaged attenuation rate

The 3-D regional attenuation is potentially useful for improving engineering response spectra models. Such ground motion prediction equations (GMPEs) generally perform regression to fit available strong motion data at specific frequencies. The path attenuation is an important term for distances greater than 50 km, and is typically formulated as the attenuation

rate multiplied by distance. To have a comparable parameter, attenuation rate ($\pi/(Qs*Vs)$) can be estimated. Synthetic t* can be calculated for any path and converted to an attenuation rate (Cq), taking into account the frequency dependence, and using $t^*=r/(QV)$ where *r* is the straight slant path.

$$Cq(f)= -\pi f^{(1-\alpha)} f_0^{\alpha}(t^*/r) \quad (5)$$

While Q acts per wavelength, Cq in GMPEs acts per distance.

For all station locations, this synthetic attenuation rate was calculated for the location of the 2014 South Napa earthquake, as shown in Figure 9a. This is not an intuitive plot because it is not directly mapping a physical parameter but instead is displaying the whole-path effect at the station end of each path. Thus it would look different for every different source location. The large variation in Cq contrasts with the simple uniform attenuation rate for California in most GMPEs. It illustrates a general 1-D Q variation as Cq is reduced for longer paths that sample high Q deeper crust. Additional spatial variation is apparent with greater attenuation through the Coast Range and particularly southeast of the hypocenter, and in the region of the Rodgers Creek fault zone.

The psuedospectral acceleration (PSA) for the 2014 M 6.0 South Napa earthquake was overpredicted by GMPEs as shown by Baltay and Boatwright (2015). For comparison to attenuation, these are normalized for 80-km distance, with factor 80/r, and plotted in Figure 9b. The pattern of largest negative residuals is broadly similar to the Cq pattern, excluding the few large positive residuals near the hypocenter. The largest negative residuals are near the hypocenter with size decreasing at greater distance, indicative of a general 1-D Q that increases with depth. Yet the decrease in residual PSA is not simply radial, with the areas of lowest residual centered southeast of the hypocenter and elongated in a northwest-southeast direction, similar to the area of high attenuation rate from 3-D Q. This includes a narrower band of large negative residuals northwest of the hypocenter, which is similar to a zone of high attenuation rate. Other factors related to source and near-surface site effects will influence PSA and also will relate to the residual pattern, contributing to specific large positive residuals such as seen south of the source. However, the general similarity of regional patterns indicates that GMPEs may be improved with more realistic attenuation rate computed for each path, rather than a single value for all paths.

The attenuation terms in GMPEs are empirically fit along with many other terms and may not be directly replaceable by 3-D Q path-dependent values, without recalculating other terms. Rietbrock et al. (2013) have included the United Kingdom (UK) 1-D Q model derived from microearthquakes in stochastic simulations to compute a regional GMPE for the UK. Yenier and Atkinson (2015) have developed a regionally adjustable generic GMPE which allows modification for regional attenuation. They define adjustable attenuation with an event term and attenuation rate, and additionally include an overall calibration factor. Hence in future work for

northern California, path-specific attenuation rates from the 3-D Q model could be incorporated prior to fitting the event terms and calibration factor in the adjustable GMPE. This would enable quantitative evaluation of how the 3-D Q model influences residuals and epistemic uncertainty in GMPEs.

CONCLUSIONS

Path attenuation t* values have been determined for P and S spectral decay, from local earthquakes throughout northern California. Using frequency dependence of 0.5, 3-D Qp and Qs models were obtained with progressive inversion and autolinking to achieve reasonable Q values throughout the model area.

The subduction region exhibits the highest Q (Qs>1200) for the strong mafic subducting slab, and the overlying forearc basin has very low Q consistent with thick marine sedimentary rocks. Below the volcanic arc, moderately low Q is imaged from 20-45 km depth, where there may be upwardly migrating fluids from the slab resulting from slab dehydration. South of the slab edge, low Q at 20-35 km depth corresponds to the slab window.

In the ~100-km wide transform fault system, the major faults tend to be characterized in the brittle crust by low Q, which may be related to broadly distributed microcracks and enhanced by fluids. In contrast, the ductile lower crust shows moderately low Q extending across the fault system, consistent with grain-size reduction from long-term high strain rate. The broad ductile shear zone extends under the northern and southern Coast Ranges and thus may be limited by the rheology of the adjacent Great Valley ophiolite basement.

The Sierra Nevada has high Q related to the igneous low porosity rock of the large batholith. High Q is also shown for the igneous Salinian block and the Bay area block between the San Andreas and Hayward faults. The Great Valley ophiolite corresponds to a prominent high Q region from 14-27 km depth, under the moderately low Q sedimentary basin, and contains deeper seismicity than the Coast Ranges.

The large variation in Q implies that the uniform Q that is used in GMPEs may be unrealistic for northern California. The pattern of path specific attenuation rate, from 3-D Q, is generally similar to the pattern of psuedospectral acceleration residuals for the South Napa earthquake. Thus future work may incorporate 3-D Q models into GMPEs.

DATA AND RESOURCES

Waveform data were obtained from the Northern California Earthquake Data Center www.ncedc.org (last accessed April 2015), and IRIS ds.iris.edu/ds/nodes/dm (last accessed February 2016). Hypocenters were obtained from the double-difference catalog (Waldhauser,

2009; http:/ddrt.ldeo.columbia.edu/DDRT, last accessed April 2015). Most figures were generated with the GMT package (Wessel and Smith, 1998; gmt.soest.hawaii.edu).

ACKNOWLEDGEMENTS

Emma Kludge assisted in data analysis. Annemarie Baltay provided the South Napa PSA data. This work was supported by the National Earthquake Hazards Reduction Program of the U.S. Geological Survey (USGS), Department of the Interior, under USGS award number G14AP00100. The manuscript benefitted from helpful reviews from Thomas Brocher and John Naliboff.

REFERENCES

Abercrombie, R. (1995), Earthquake source scaling relationships from -1 to 5 ML using seismograms recorded at 2.5-km depth, *J. Geophys. Res*, *100*, 24,015-024,036.

Abrahamson, N. A., W. J. Silva, and R. Kamai (2014), Summary of the ASK14 ground-motion relation for active crustal regions, *Earthq. Spectra*, *30*, 1025-1055, doi:10.1193/070913EQS198M.

Argus, D. F., and R. G. Gordon (2001), Present tectonic motion across the Coast Ranges and San Andreas fault in central California, *Geo. Soc. Amer. Bull.*, *113*, 1580-1592.

Aizawa, Y., A. Barnhoorn, U. H. Faul, J. D. Fitzgerald, I. Jackson, and I. Kovacs (2008), Seismic properties of Anita Bay dunite: an exploratory study of the influence of water, *J. Petrology*, *19*, 841-855.

Asano, Y., and A. Hasegawa (2004), Imaging the fault zones of the 2000 western Tottori earthquake by a new inversion method to estimate three-dimensional distribution of the scattering coefficent, *J. Geophys. Res*, *109*, B06306,doi:06310.01029/02003JB002761.

Audet, P. (2015), Layered crustal anisotropy around the San Andreas fault new Parkfield, California, *J. Geophys. Res*, *120*, 3527-3543, doi:10.1002/2014JB011821.

Baltay, A. S., and J. Boatwright (2015), Ground-motion observations of the 2014 South Napa earthquake, *Seis. Res. Lett.*, *86*, 355-360, doi:10.1785/0220140232.

Beaudoin, B. C., M. Magee, and H. Benz (1994), Crustal velocity structure north of the Mendocino triple junction, *Geophys. Res. Let.*, *21*, 2319-2322.

Bennington, N., C. Thurber, and S. Roecker (2008), Three-dimensional seismic attenuation structure around the SAFOD site, Parkfield, California, *Bull. Seimol. Soc. Am.*, *98*, 2934-2947.

Beyer, L. A. (1988), Summary of geology and petroleum plays used to assess undiscovered recoverable petroleum resources of Sacramento Basin province, California, *U. S. Geol. Surv. Open-File Rep. 88-450*, 64 pp.

Blake, M. C., A. S. Jayko, R. J. McLaughlin, and M. B. Underwood (1988), Metamorphic and tectonic evolution of the Franciscan Complex, northern California, in *Metamorphism and*

crustal evolution of the Western United States, Rubey Vol. 7, edited by W. G. Ernst, pp. 1035-1060, Prentice-Hall, Englewood Cliffs, N. J.

Brocher, T. M., Baltay, A. S., Hardebeck, J. L., Pollitz, F. F., Murray, J. R., Llenos, A. L., Schwartz, D. P., Blair, J. L., Dawson, T. E., Hudnut, K. W., et al. (2015), The Mw 6.0 24 August 2014 South Napa earthquake, *Seis. Res. Lett.*, *86*, 309-326, doi:10.1785/0220150004.

Brune, J. N. (1970), Tectonic stress and the seismic shear waves from earthquakes, *J. Geophys. Res.*, *75*, 4997-5009.

Clarke, S. H., Jr. (1992), Geology of the Eel river basin and adjacent region: implications for late Cenozoic tectonics of the southern Cascadia subduction zone and Mendocino triple junction, *Am. Assoc. Pet. Geol. Bull.*, *76*, 199-224.

Eberhart-Phillips, D., Reyners, M., Chadwick, M. and Stuart, G. (2008b), Three-dimensional attenuation structure of the Hikurangi subduction zone in the central North Island, New Zealand, *Geophys. J . Int.*, *174*, 418-434.

Eberhart-Phillips, D., S. Bannister, and S. Ellis (2014a), Imaging P and S Attenuation in the Termination Region of the Hikurangi Subduction Zone, New Zealand, *Geophys. J . Int.*, *198*, 516-536, doi: 510.1093/gji/ggu1151.

Eberhart-Phillips, D., and M. Chadwick (2002), Three-dimensional attenuation model of the shallow Hikurangi subduction zone in the Raukumara Peninsula, New Zealand, *J. Geophys. Res.*, *107*, doi:10.1029/2000JB000046.

Eberhart-Phillips, D., M. Chadwick, and S. Bannister (2008a), Three-dimensional attenuation structure of central and southern South Island, New Zealand, from local earthquakes, *J. Geophys. Res.*, *113*(B05308), doi:10.1029/2007JB005359.

Eberhart-Phillips, D., and A. J. Michael (1993), Three-dimensional velocity structure, seismicity, and fault structure in the Parkfield region, central California, *J. Geophys. Res.*, *98*, 15,737-715,758.

Eberhart-Phillips, D., and M. Reyners (2012), Imaging the Hikurangi plate interface region with improved local-earthquake tomography, *Geophysical J.Int.*, *190*, 1221-1242, doi: 1210.1111/j.1365-1246X.2012.05553.x.

Eberhart-Phillips, D., C. Thurber, and J. B. Fletcher (2014b), Imaging P and S Attenuation in the Sacramento-San Joaquin Delta region, northern California, *Bull. Seism. Soc. Am.*, *104*, 2322-2336, doi: 2310.1785/0120130336.

Ellis, S., Beavan, J., Eberhart-Phillips, D., and B. Stockhert (2006), Simplified models of the Alpine fault seismic cycle: stress transfer in the mid-crust, *Geophys. J. Int.*, *166*(doi:1111/j.1365-246X.2006.02917.x), 386-402.

Fletcher, J. B., and J. Boatwright (2013), Site response and basin waves in the Sacramento-San Joaquin Delta, California, *Bull. Seism. Soc. Am.*, *103*, 196-210.

Fletcher, J. B., K. J. Seats, J. F. Lawrence, and J. Erdem (2016), Tomographic Rayleigh-wave Group Velocities in the Central Valley, California Centered on the Sacramento/San Joaquin Delta, *J. Geophys. Res*, *121*, 2429-2446, doi:10.1002/2015JB012376.

Frankel, A. (1991), Mechanisms of seismic attenuation in the crust: scattering and anelasticity in New York state, South Africa, and southern California, *J. Geophys. Res.*, *96*, 6269-6289.

Furlong, K. P., and S. Y. Schwartz (2004), Influence of the Mendocino triple junction on the tectonics of coastal California, *Annu. Rev. Earth Planet. Sci.*, *32*, 403-433, doi:10.1146/annurev.earth.32.101802.120252.

Gilbert, H., Y. Yang, D. W. Forsyth, C. H. Jones, T. J. Owens, G. Zandt, and J. C. Stachnik (2012), Imaging lithospheric foundering in the structure of the Sierra Nevada, *Geosphere*, *8*, 1310-1330, doi:10.1130/GES00790.1.

Godfrey, N., B. C. Beaudoin, S. L. Klemperer, and Mendocino_Working_Group (1997), Ophiolitic basement to the Great Valley forearc basin, northern California, from seismic and gravity data: Implications for crustal growth at the North American continental margin, *Geol. Soc. Am. Bull.*, *109*, 1536-1562.

Godfrey, N. J., and S. L. Klemperer (1998), Ophiolitic basement to a forearc basin and implications for continental growth: the Coast Range/Great Valley ophiolite, California, *Tectonics*, *17*, 558-570.

Hill, D. P. (2006), Unrest in Long Valley caldera, California, 1978-2004, in *Mechanisms of Activity and Unrest at Large Calderas, Spec. Pub. 269*, edited by C. DeNatle and C. R. J. Kilburn, pp. 1-24, Geological Society of London.

Holbrook, W. S., T. M. Brocher, U. S. ten Brink, and J. A. Hole (1996), Crustal structure of a transform plate boundary: San Francisco Bay and the central California continental margin, *J. Geophys. Res*, *101*, 22,311-322,334.

Hopps, T., and E. Horan (1983), Subsurface stratigraphy: Eel river basin, in *Pacific Sec. 1983 Ann. Mtg.*, edited by R. I. Hester and D. F. Hallinger, Am. Ass. Petro. Geol., Sacramento.

Ingersoll, R. V. (1982), Initiation and evolution of the Great Valley forearc basin of northern and central California, U.S.A., *Geol. Soc. London Spec. Publ.*, *10*, 459-467

Irwin, W. P. (1990), Geology and plate-tectonic development, in *The San Andreas Fault System, California*, edited by R. E. Wallace, U. S. Geological Survey, Washington.

Jackson, I., J. D. Fitzgerald, U. H. Faul, and B. H. Tan (2002), Grain-size-sensitive seismic wave attenuation in polycrystalline olivine, *J. Geophys. Res.*, *107*, ECV5 doi:1029/2001JB001225.

Karato, S. I. (2012), On the origin of the asthenosphere, *Earth Planet. Sci. Lett.*, *321-322*, 95-103.

Kenner, S. J., and P. Segall (2003), Lower crustal structure in northern California: implications from strain rate variations following the 1906 San Francisco earthquake, *J. Geophys. Res*, *108*, doi:10.1029/2001JB000189003.

Koulakov, I., D. Bindi, S. Parolai, H. Grosser, and C. Milkereit (2010), Distribution of seismic velocities and attenuation in the crust beneath the North Anatolian Fault (Turkey) from local earthquake tomography, *Bull. Seism. Soc. Am.*, *100*, 207-224.

Lai, V. H., R. Graves, S. Wei, and D. Helmberger (2015), Evidence for fast seismic lid structure beneath the Californian margin and its implication on regional plate deformation *AGU Fall Meeting 2015*, S11B-08.

Lees, J., and G. Lindley (1994), Three-dimensional attenuation tomography at Loma Prieta: inverting t* for Q, *J. Geophys. Res.*, *99*, 6843-6863.

Levander, A., T. J. Henstock, A. S. Meltzer, B. C. Beaudoin, A. M. Trehu, and S. L. Klemperer (1998), Fluids in the lower crust following Mendocino triple junction migration: Active basaltic intrusion? , *Geology*, *26*, 171-174.

Lin, G. (2014), Three-dimensional compressional wave attenuation tomography for the crust and uppermost mantle of Northern and central California, *J. Geophys. Res*, *119*, 3462-3477, doi:10.1002/2013JB010621.

Lin, G. (2015), Seismic velocity structure and earthquake relocation for the magmatic system beneath Long Valley Caldera, eastern California, *J. Volc. Geotherm. Res.*, *296*, 19-30.

Lin, G., C. H. Thurber, H. Zhang, E. Hauksson, P. M. Shearer, F. Waldhauser, T. M. Brocher, and J., and Hardebeck (2010), A California statewide three-dimensional seismic velocity model from both absolute and differential times, *Bull. Seism. Soc. Am.*, *100*, 225-240; DOI: 210.1785/0120090028.

Liu, K., A. Levander, Y. Zhai, R. W. Porritt, and R. M. Allen (2012), Asthenospheric flow and lithospheric evolution near the Mendocino Triple Junction, *Earth Planet. Sci. Lett.*, *323*, 60-71.

Ma, S. (2008), A physical model for widespread near-surface and fault zone damage induced by earthquakes, *Geochem. Geophys. Geosytems*, *9*, Q11009, doi:11010.11029/12008GC002231.

McKee, E. H., W. A. Duffield, and R. J. Stern (1983), Late Miocene and early Pliocene basaltic rocks and their implications for crustal structure, northeastern California and South-central Oregon, *Geo. Soc. Amer. Bull.*, *94*, 292-304, doi:10.1130/0016-7606(1983)94.

McPhee, D. K., V. E. Langenheim, S. Hartzell, R. J. McLaughlin, B. T. Aagaard, R. C. Jachens, and C. McCabe (2007), Basin structure beneath the Santa Rosa plain, northern California: implications for damage caused by the 1969 Santa Rosa and 1906 San Francisco earthquakes, *Bull. Seimol. Soc. Am.*, *97*, 1449-1457, doi:10.1785/200060269.

Michelini, A., and T. V. McEvilly (1991), Seismological studies at Parkfield: I. Simultaneous inversion for velocity structure and hypocenters using cubic b-splines parameterization, *Bull. Seismol. Soc. Am.*, *81*, 524-552.

Mitchell, T. M., and D. R. Faulkner (2008), Experimental measurements of permeability evolution during triaxial compression of intially intact crystalline rocks and implications for fluid flow in fault zones, *J. Geophys. Res.*, *113*, B11412, doi:11410.11029/12008JB005588.

Moores, E. M., J. Wakabayashi, and J. R. Unruh (2002), Crustal-scale cross-section of the U.S. Cordillera, California and beyond, its tectonic significance, and speculations on the Andean orogeny, *Int. Geology Rev.*, *44*, 479-500.

Norris, R. J., Cooper, A. F. (2003), Very high strains recorded in mylonites along the Alpine Fault, New Zealand: implications for the deep structure of plate boundary faults, *J. Struc. Geol.*, *25*, 2141-2157.

Page, B. M. (1981), The southern Coast Ranges, in *The geotectonic development of California (Rubey Volume 1)*, edited by W. G. Ernst, pp. 329-417, Prentice-Hall, Englewood Cliffs, NJ.

Peacock, S., C. McCann, J. Sothcott, and T. R. Astin (1994), Experimental measurements of seismic attenuation in microfractured sedimentary rock, *Geophysics*, *59*, 1342-1351.

Phillips, W. S., and R. J. Stead (2008), Attenuation of Lg in the western US using the USArray, *Geophys. Res. Lett.*, *35*, DOI: 10.1029/2007GL032926.

Platt, J. P., and W. M. Behr (2011), Grainsize evolution in ductile shear zones: Implications for strain localization and the strength of the lithosphere, *J. Structural Geol.*, *33*, 537-550.

Rietbrock, A. (2001), P-wave attenuation structure in the fault area of the 1995 Kobe earthquake, *J. Geophys. Res.*, *106*, 4141-4154.

Rietbrock, A., F. Strasser, and B. Edwards (2013), A stochastic earthquake ground-motion prediction model for the United Kingdom, *Bull. Seism. Soc. Am.*, *103*, 57-77.

Schweickert, R. A. (1981), Tectonic development of the Sierra Nevada Range, in *The geotectonic development of California (Rubey Volume 1)*, edited by W. G. Ernst, pp. 87-131, Prentice-Hall, Englewood Cliffs, NJ.

Scherer, H. H., and W. G. Ernst (2008), North Fork terrane, Klamath Mountains, California: Geologic, geochemical, and geochronologic evidence for an early Mesozoic forearc, in *Ophiolites, Arcs, and Batholiths: A Tribute to Cliff Hopson, Geol. Soc. Am. Spec. Pap. 438*, edited by J. E. Wright and J. W. Shervais, pp. 289-309.

Stachnik, J. C., G. A. Abers, and D. H. Christensen (2004), Seismic attenuation and mantle wedge temperatures in the Alaska subsuction zone, *J. Geophys. Res.*, *109*(doi:10.1029/2004JB003018).

Tape, C., A. Plesch, J. H. Shaw, and H. Gilbert (2012), Estimating a continuous Moho surface for the California unified velocity model, *Seis. Res. Lett.*, *83*, 728-735, doi:10.1785/0220110118.

Teel, A. C. (2012), Seismic Tomography of the Sacramento – San Joaquin River Delta: Joint P-wave/Gravity and Ambient Noise Methods, Ph.D. thesis, 95 pp, Univ. Wisconsin-Madison, Madison.

Thurber, C., and D. Eberhart-Phillips (1999), Local earthquake tomography with flexible gridding, *Computers and Geoscience*, *25*, 809-818.

Thurber, C., H. Zhang, T. M. Brocher, and V. Langenheim (2009), Regional three-dimensional seismic velocity model of the crust and uppermost mantle of northern California, *J. Geophys. Res*, *114*, B01304, doi:01310.01029/02008JB005766.

Waldhauser, F. (2009), Near real-time double-difference event location using long-term seismic archives, with application to northern California, *Bull. Seism. Soc. Am.*, *99*, 2736-2748.

Wang, Y.-J., K.-F. Ma, F. Mouthereau, and D. Eberhart-Phillips (2009), Three dimensional Qp- and Qs-Tomography beneath Taiwan Orogenic Belt: Implications for Tectonic and Thermal Structure, *Geophys. J . Int.*, doi: 10.1111/j.1365-1246X.2009.04459.x.

Wessel, P. and W. H. F. Smith (1998). New version of the generic mapping tools released, *Eos Trans. AGU*, 79, 579.

Wentworth, C. M., Fisher, G. R., Levine, P., and Jachens, R. C. (1995). The surface of crystalline basement, Great Valley and Sierra Nevada, California: A digital map database, *U.S. Geol. Surv. Open-File Rep. 95-96*, v. 1.11, 18 pp.

White, S. H., Burrows, S.E., Carreras, J., Shaw, N.D., Humphreys, F.J. (1980), On mylonites in ductile shear zones, *J. Struc. Geol.*, *2*, 175-187.

Winkler, K. W., and W. F. Murphy_III (1995), Acoustic velocity and attenuation in porous rocks, in *Rock physics and phase relations: A handbook of physical constants*, edited by T. J. Ahrens, pp. 20-34, AGU, Washington DC.

Yenier, E., and G. M. Atkinson (2015), Regionally adjustable generic ground-motion prediction equation based on equivalent point-source simulations: application to central and eastern North America, *Bull. Seimol. Soc. Am.*, *105*, 1989-2009, doi:10.1785/0120140332.

Yikilmaz, M. B., D. L. Turcotte, O. Beketova, L. H. Kellogg, and J. B. Rundle (2015), Earthquake Cycles on the San Andreas Fault System in Northern California, *Int.l Assoc. Geodesy Symposia*, 1-7, doi:10.1007/1345_2015_203.

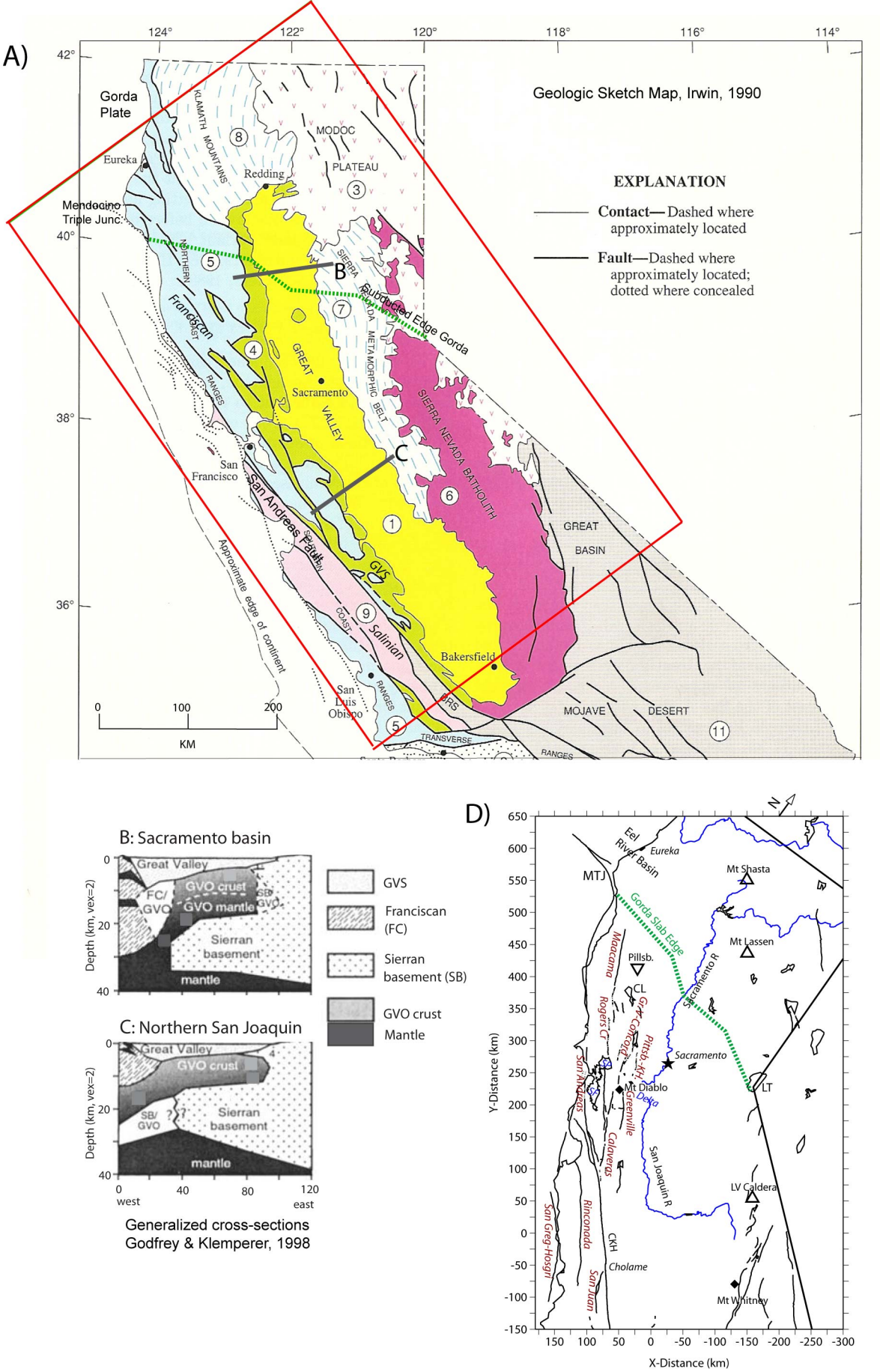

Figure 1. (a) Northern California study area (box) with geologic sketch map of California, (Irwin, 1990). Dashed line shows subducted edge of Gorda plate (Liu et al., 2012). Units: 1, Great Valley alluvium; 3, Cenozoic volcanics of Modoc Plateau; 4, Great Valley sequence; 5, Franciscan assemblage; 6, Sierra Nevada batholith – dominantly Cretaceous granitic; 7, Sierra Nevada metamorphic belt, including volcanic arc, mélange and plutons; 8, Klamath Mountains; 9, Salinian block – dominantly Cretaceous plutons. b-c) Generalized cross-sections (Godfrey and Klemperer, 1998) of the obducted Great Valley opliolite (GVO) underlying the Sacramento (B) and San Joaquin (C) basins. d) Plot of the inversion grid area with faults, major rivers, volcanic centers. CKH, Coalinga-Kettleman Hills; CL, Clear Lake; LT, Lake Tahoe; SF, San Francisco Bay; SP, San Pablo Bay.

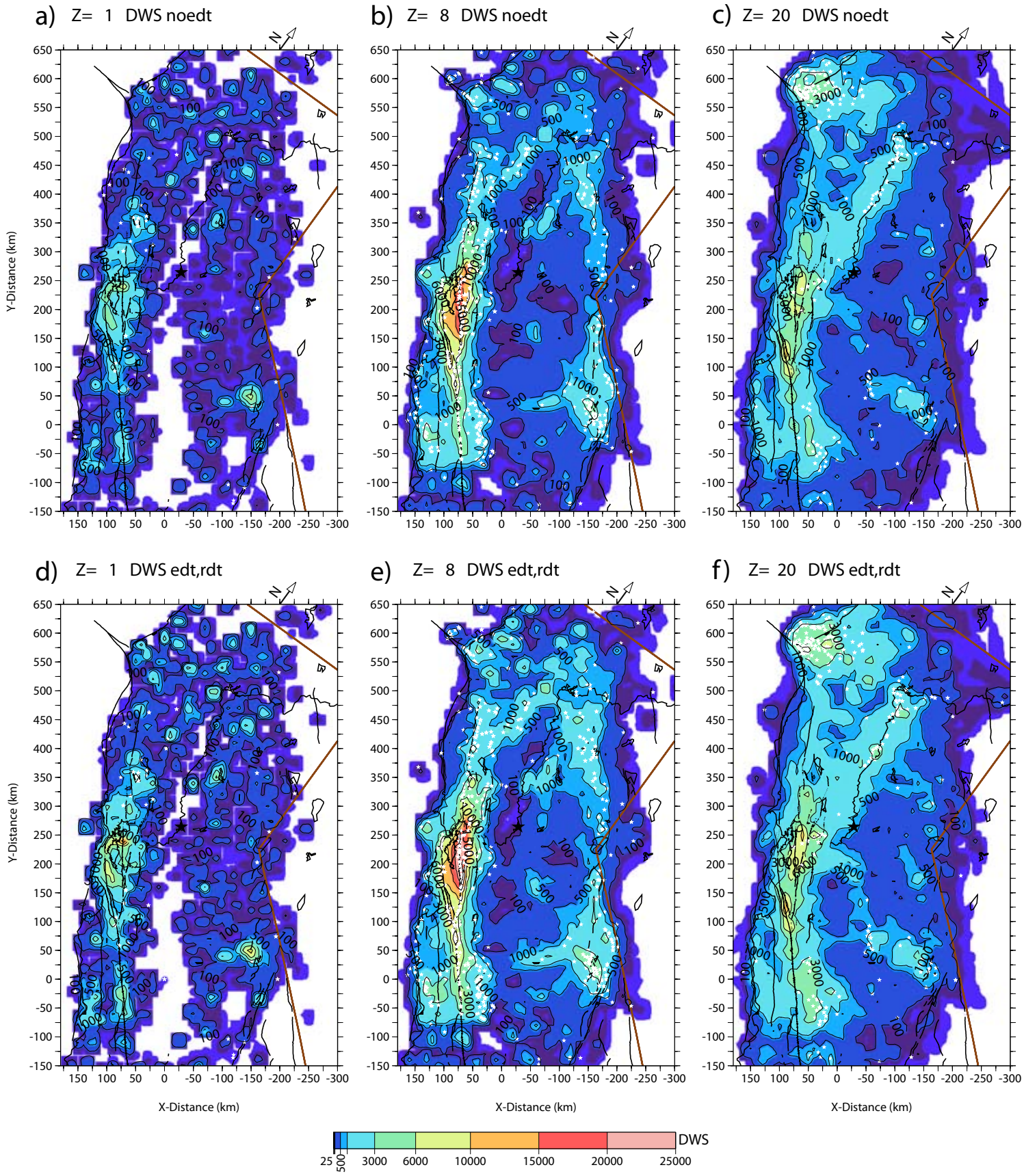

Figure 3. Data coverage at various depths (1, 8, 20 km) shown by derivative weight sum (DWS) on the 10-km grid. Upper plots (a-c) show the DWS without *rdt* or *edt* data, compared to lower plots (d-f) which include *rdt* and *edt* data, to improve resolution. White stars, inversion hypocenters near each depth. The color version of this figure is available only in the electronic edition.

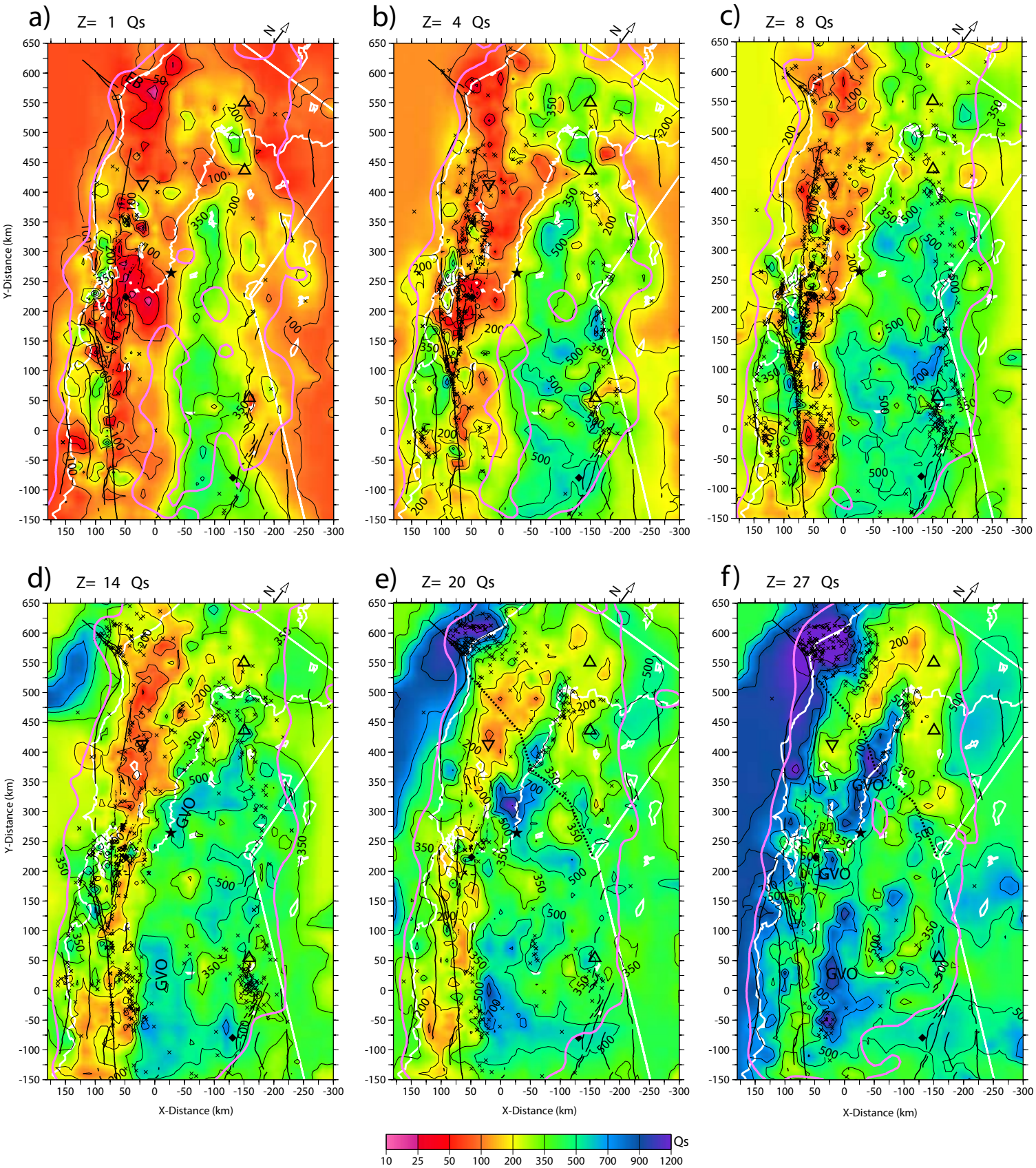

Figure 4. Results for 3-D Qs at selected depths: (a)1, (b) 4, (c) 8, (d) 14, (e) 20, (d) 27. Pale lines indicate the region of adequate data from the SF= 3.5 (SF shown in Figure S2). Inversion hypocenters near each depth are 'X'. White lines shows state line, coast; black lines show faults; triangles show volcanic features. EB, Eel River Basin; GVO, Great Valley Ophiolite. See basemaps in Figure 1 for labels and geologic features. The color version of this figure is available only in the electronic edition.

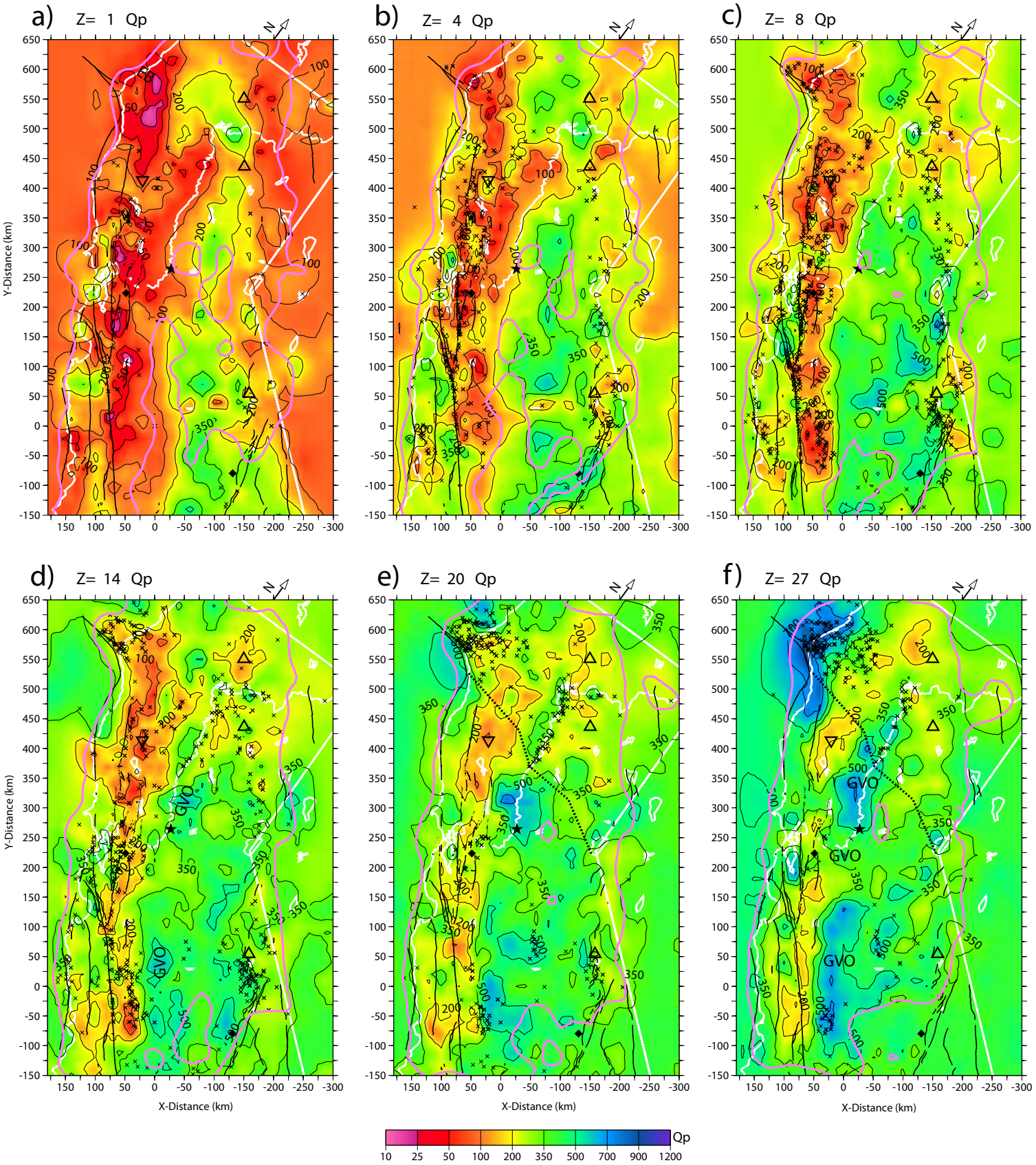

Figure 5. Results for 3-D Qp at selected depths: (a) 1, (b) 4, (c) 8, (d) 14, (e) 20, (d) 27. Pale lines indicate the region of adequate data from the SF= 3.5 (SF shown in Figure S3). Inversion hypocenters near each depth are 'X'. White lines shows state line, coast; black lines show faults; triangles show volcanic features. EB, Eel River Basin; GVO, Great Valley Ophiolite. See basemaps in Figure 1 for labels and geologic features. The color version of this figure is available only in the electronic edition.

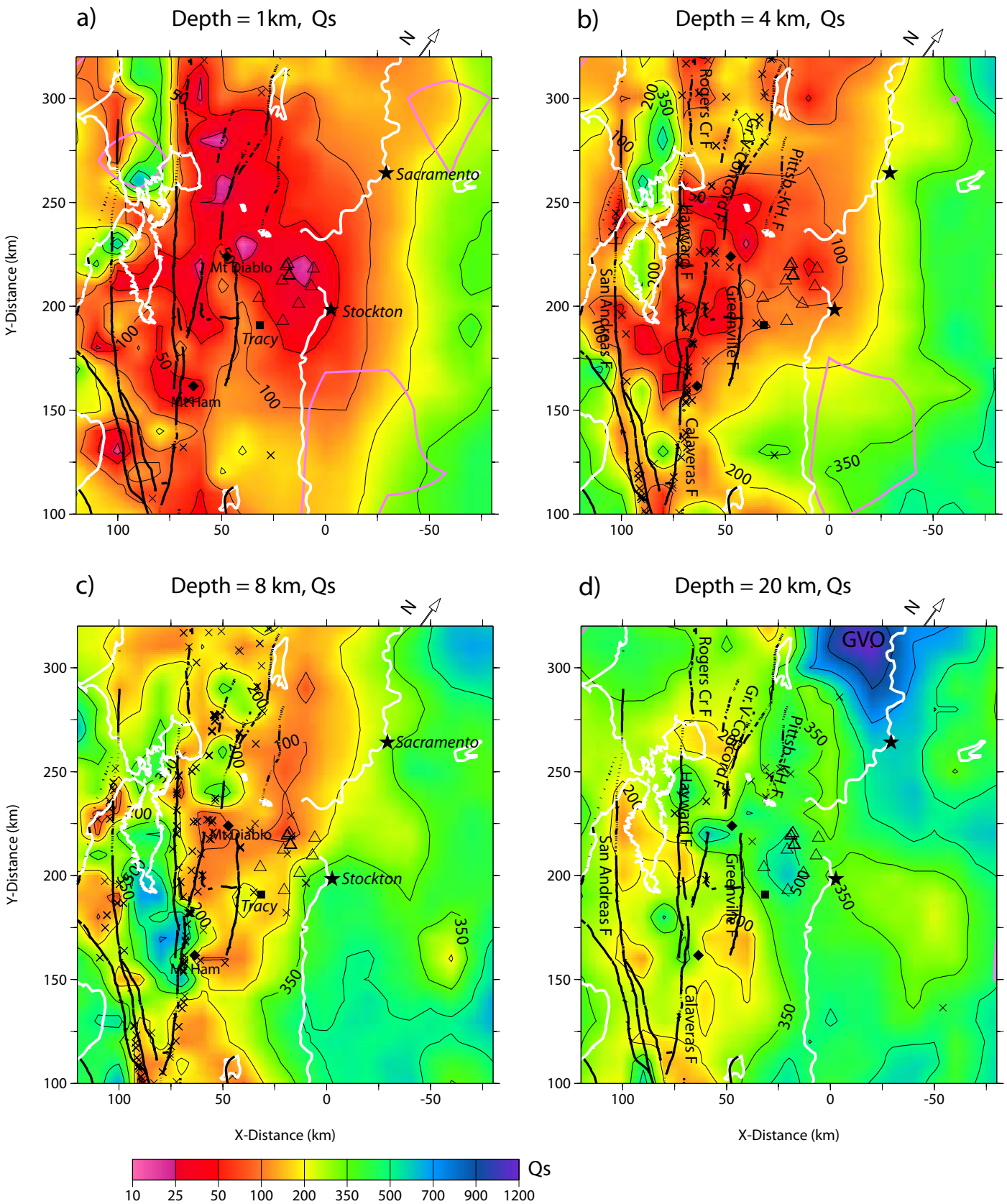

Figure 6. Results for 3-D Qs in the SF Bay area and Delta region at selected depths: (a)1, (b) 4, (c) 8, (d) 20. Inversion hypocenters near each depth are 'X'. White lines shows coast and rivers, black lines show faults, towns and features are labeled. Pale lines indicate the region of adequate data from the SF= 3.5 (SF shown in Figure S2).

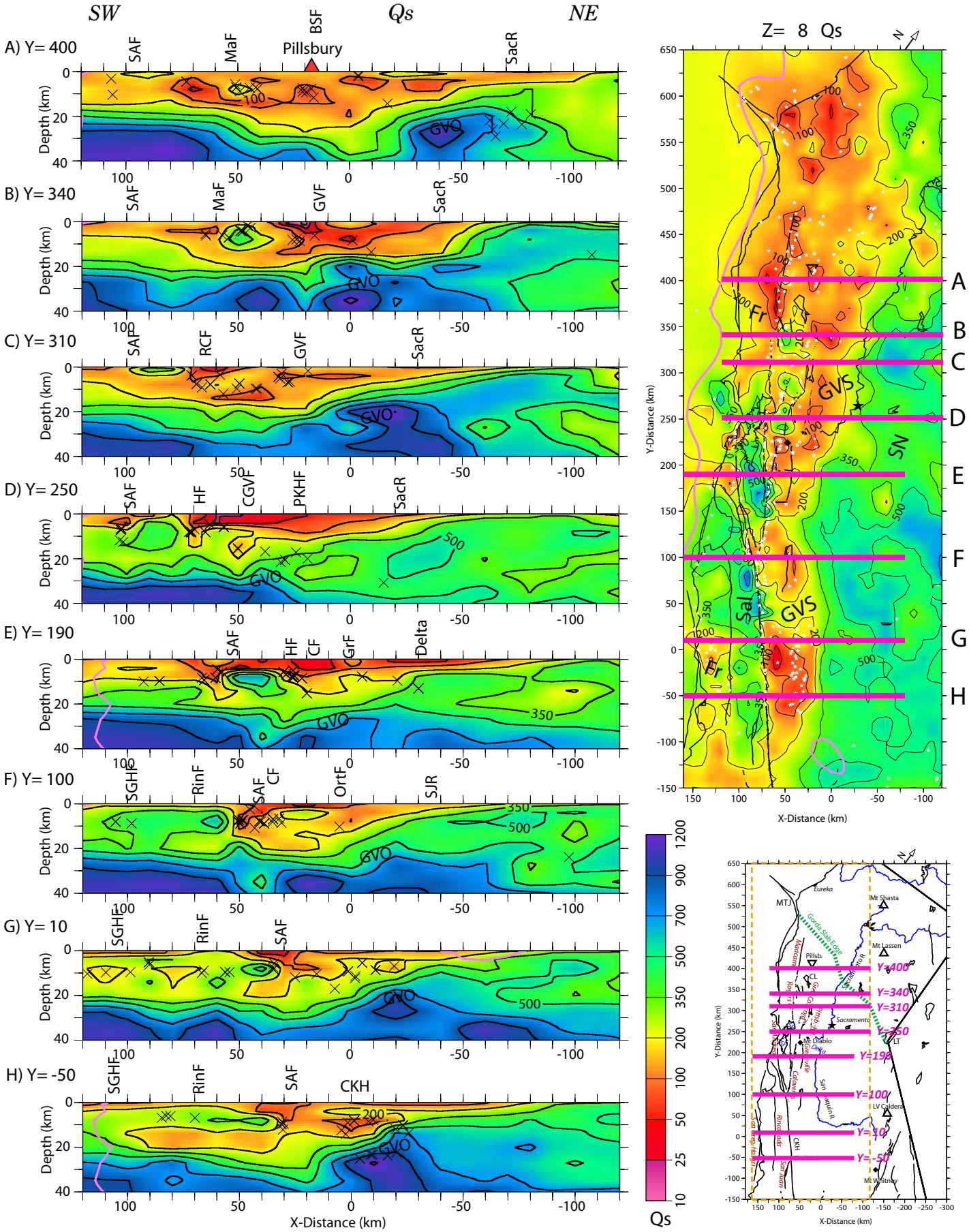

Figure 7. Cross-sections of the 3-D Qs model for y-sections indicated on 8-km depth Qs and the map inset. Faults: SAF, San Andreas; MaF, Maacama; BSF, Bartlett Springs; RCF, Rogers Creek; CGVF, Concord-Green Valley; HF, Hayward; PKHF, Pittsburgh-Kirby Hills; CF, Calaveras; GrF, Greenville; SGHF, San Gregorio-Hosgri; RinF, Rinconada; OrtF, Ortigalita. Rivers: SacR, Sacramento; SJR, San Joaquin. CKH, Coalinga-Kettleman Hills; Fr, Franciscan; GVO, Great Valley Ophiolite; GVS, Great Valley sequence; Sal, Salinian; SN, Sierra Nevada. Pale lines indicate the region of adequate data from the SF= 3.5. Inversion hypocenters are 'X'

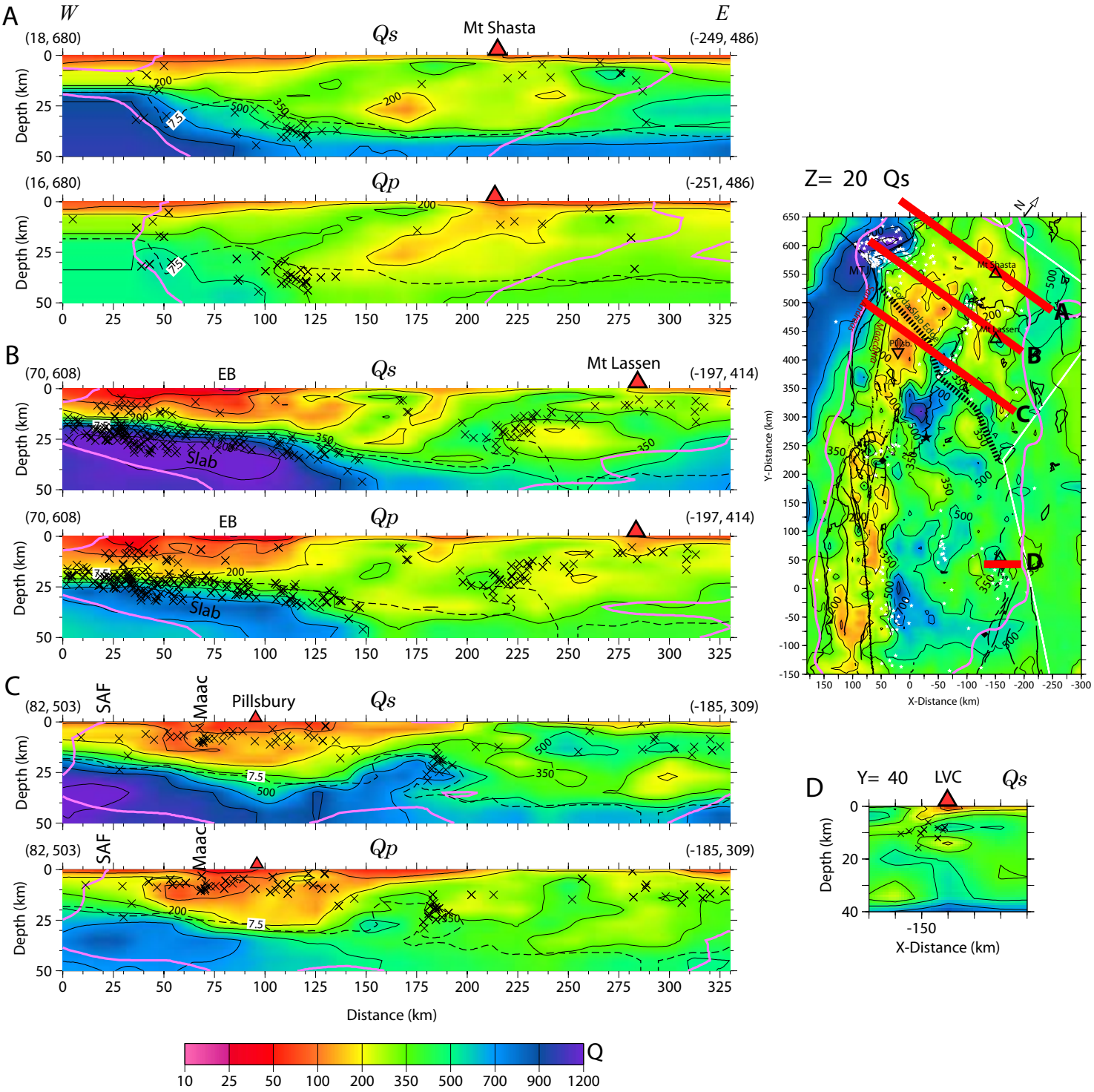

Figure 8. Cross-sections of the 3-D Qs and Qp model for profiles across the subduction region and Long Valley Caldera, as indicated in map inset. Faults: SAF, San Andreas; MaF, Maacama. EB, Eel River Basin; LCV, Long Valley Caldera. Pale lines indicate the region of adequate data from the SF= 3.5. Inversion hypocenters are 'X'. Dashed lines shows 7.5 km/s Vp contour

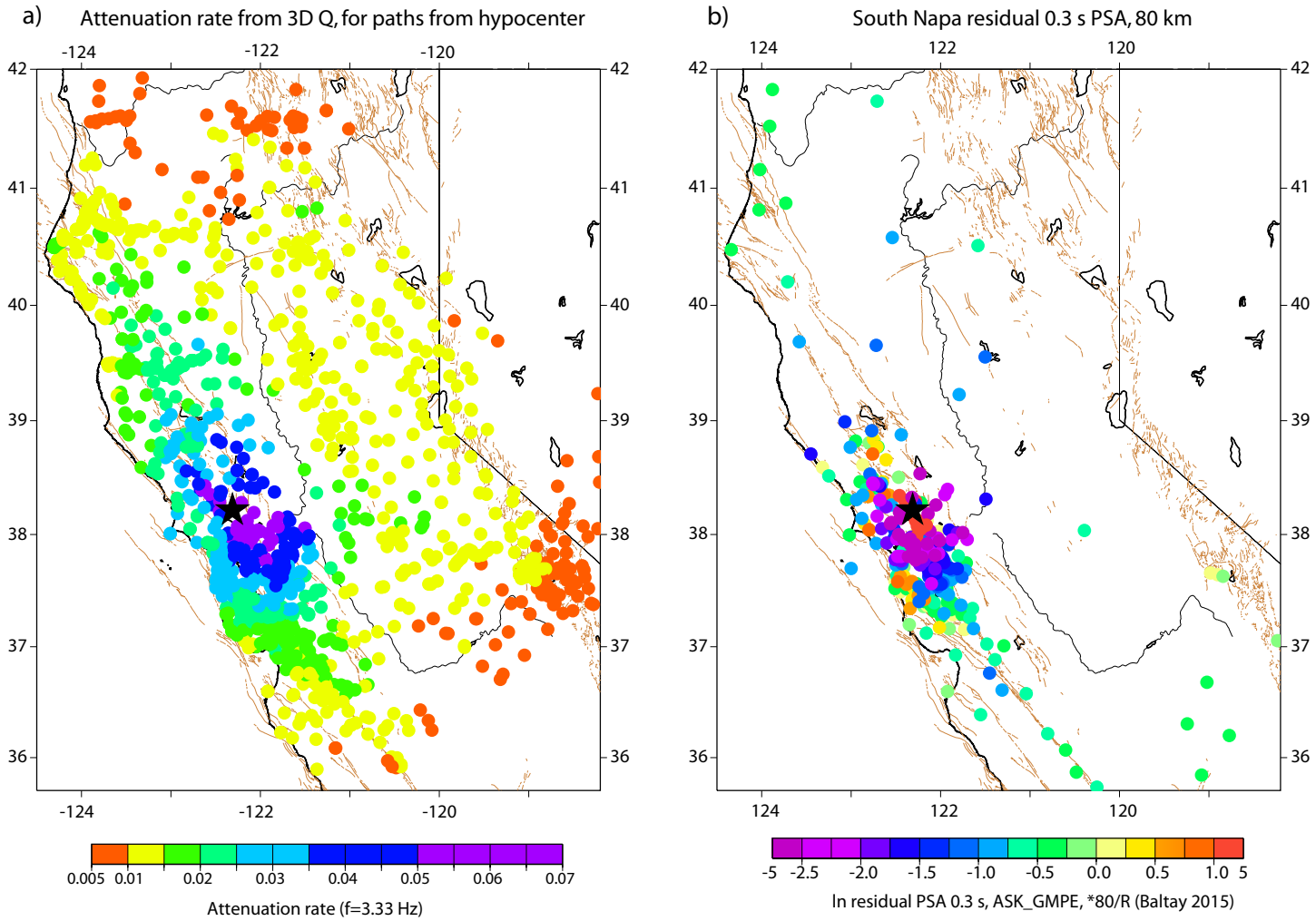

Figure 9. Comparison of patterns from South Napa source. a) Attenuation rate from 3-D Qs, computed with synthetic t* along paths from the hypocenter. b) Residuals relative to GMPE (Abrahamson et al., 2014) of psuedospectral acceleration at 0.3 s period, from Baltay and Boatwright (2015), normalized to 80-km distance.

Supplemental Material - Figure S1

Click here to download Supplemental Material (Main Page, Tables, Figures)
FigS1_cspec20100107tstar6_2.jpg

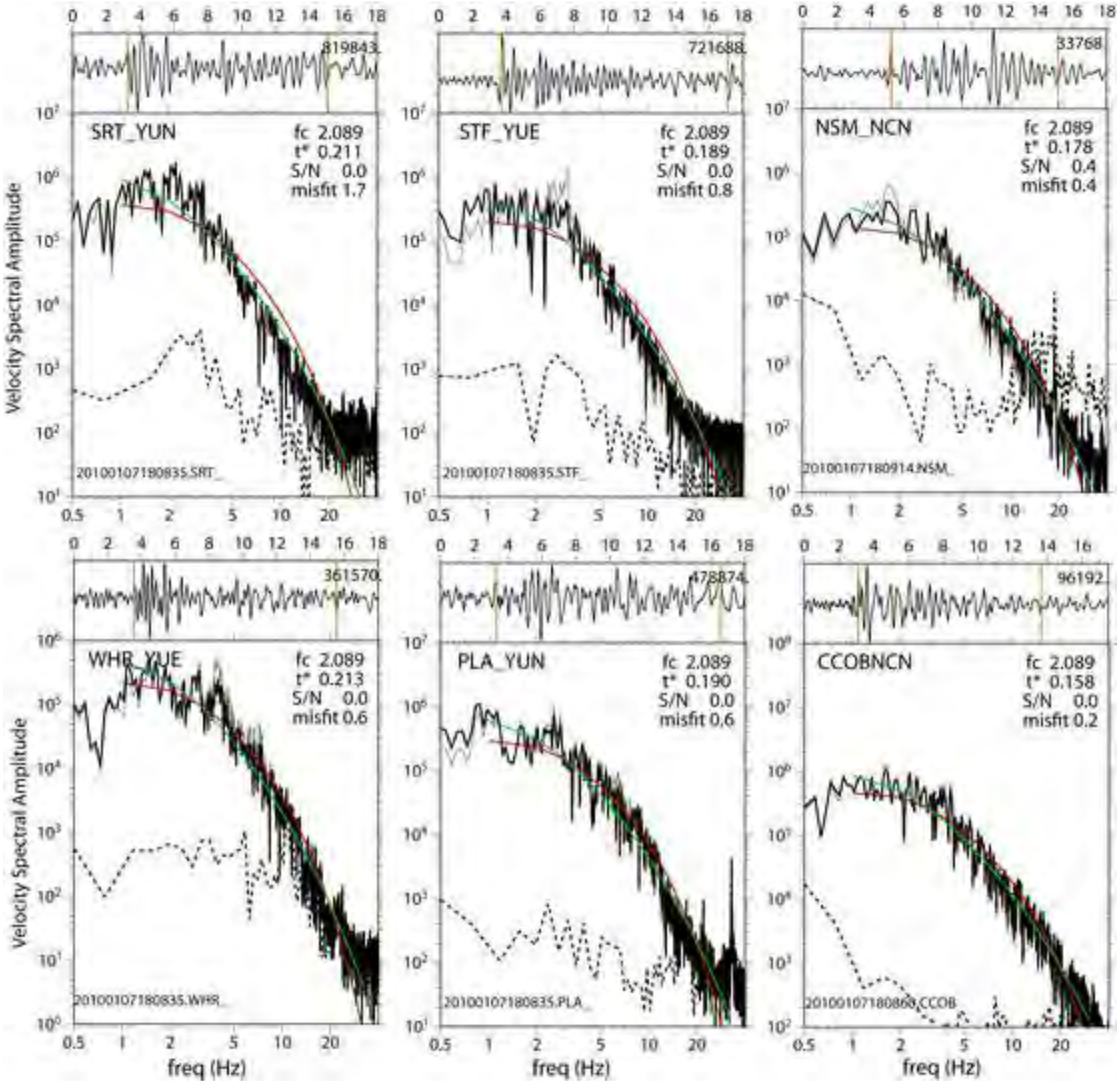

Supplemental Material - Figure S2

Click here to download Supplemental Material (Main Page, Tables, Figures) FigS2_SFQs1.jpg

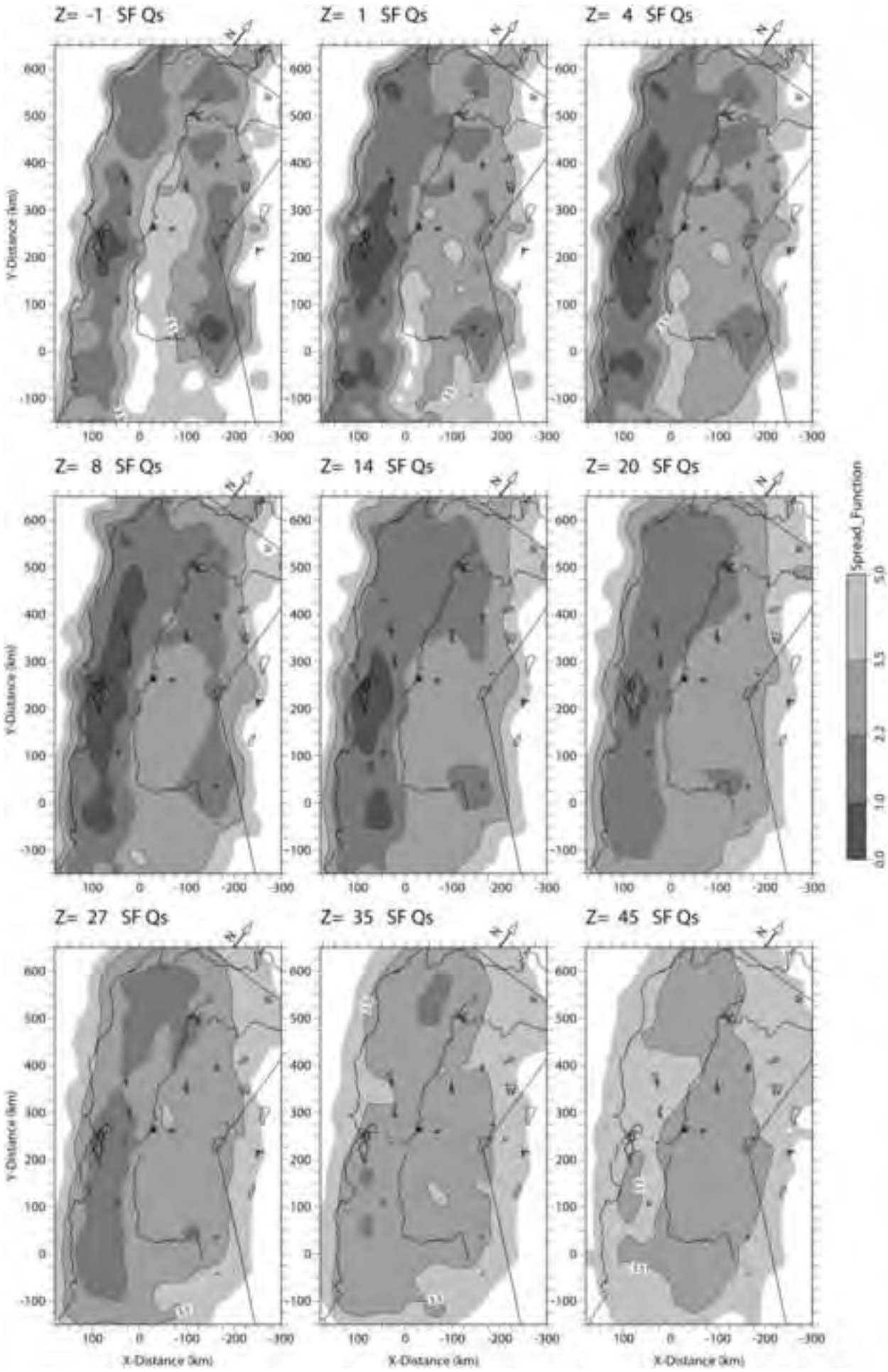

Supplemental Material - Figure S3

Click here to download Supplemental Material (Main Page, Tables, Figures) FigS3_SFQp1.jpg

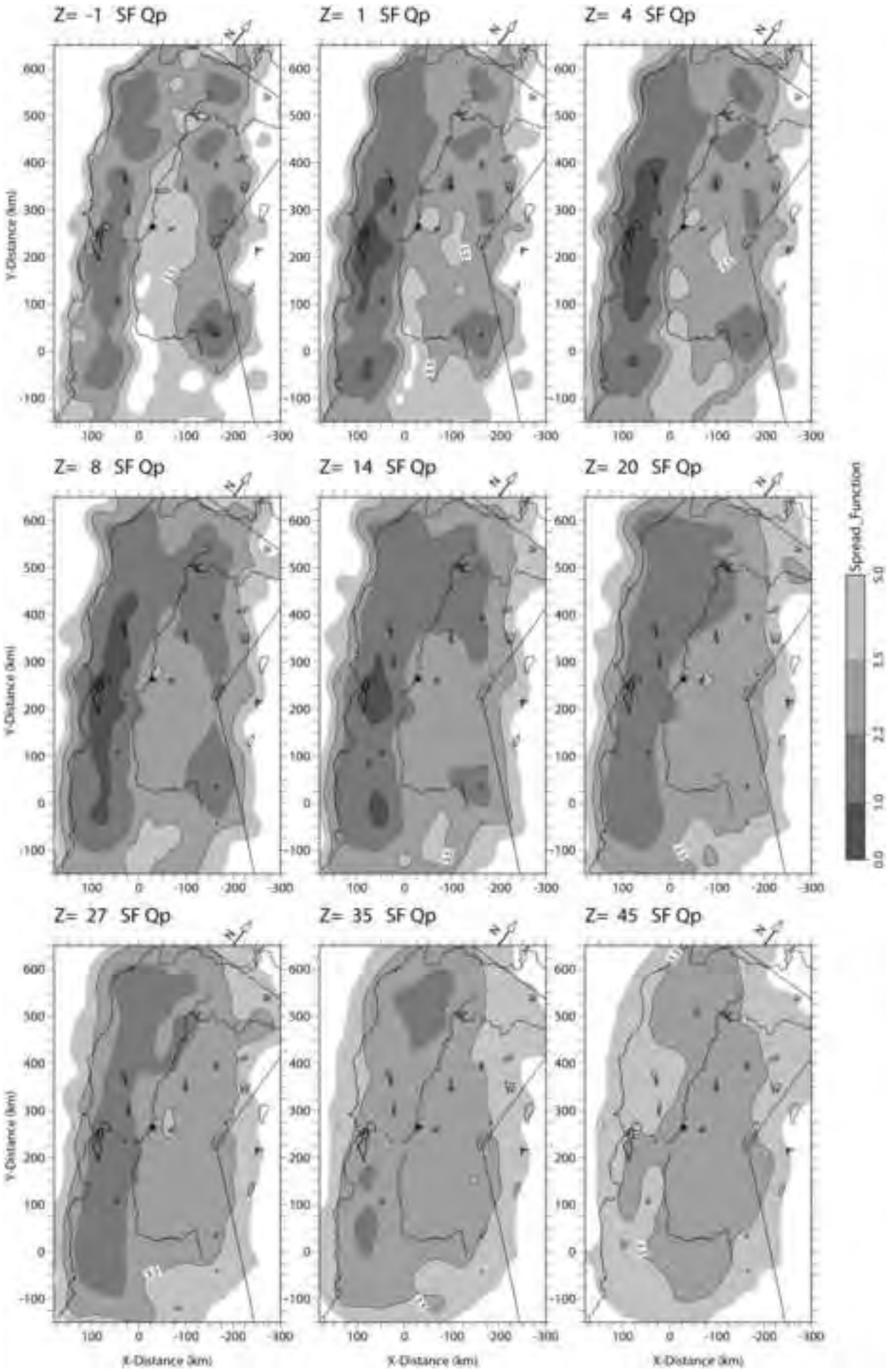

Click here to download Supplemental Material (Main Page, Tables, Figures)
FigS4_SPtsdl_1.jpg

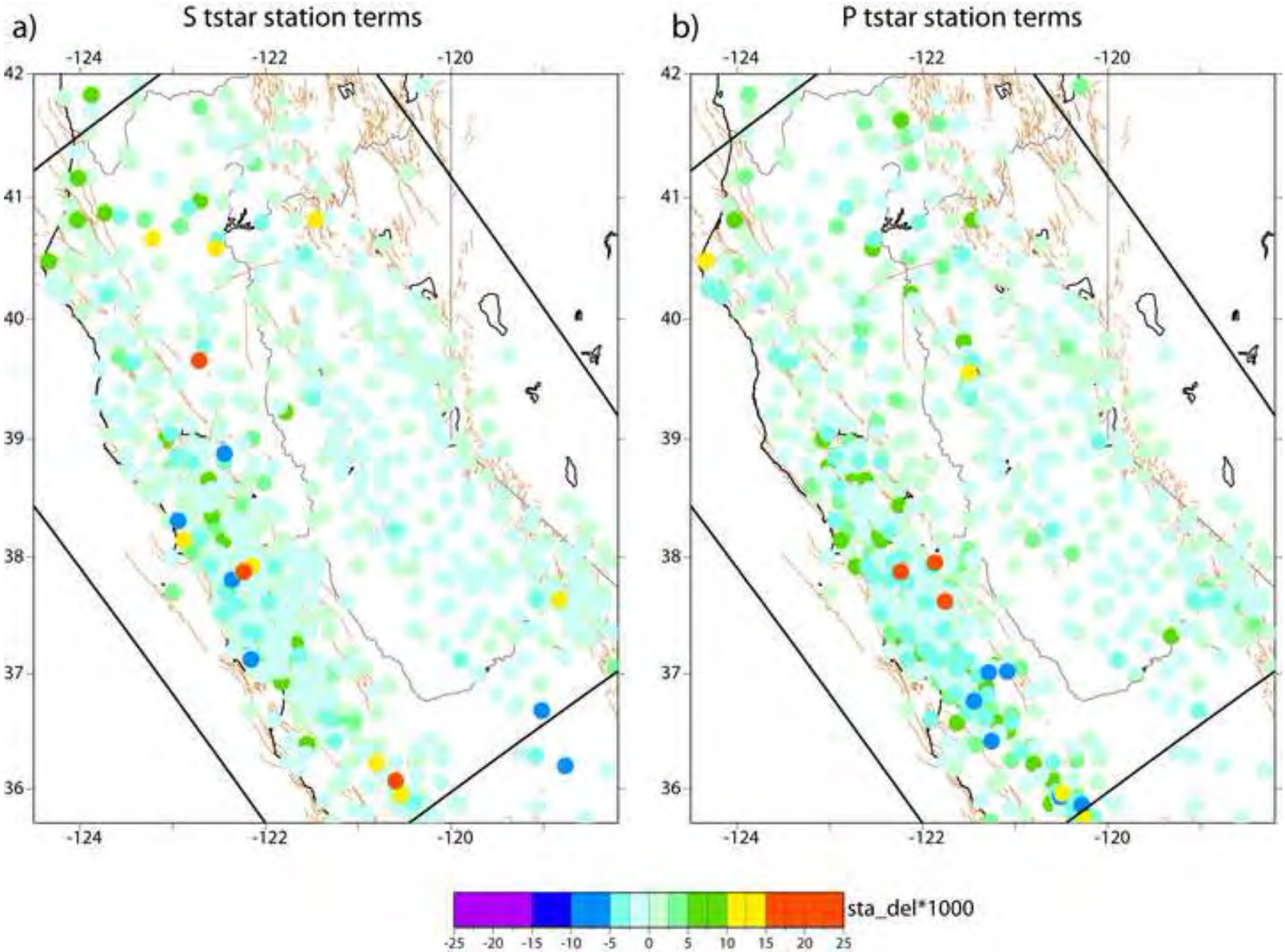

Click here to access/download
Supplemental Material (All Other Files, i.e. Movie, Zip, tar)
NCQ_Eberhart_Esuppl_table.csv